Carbohydrate Polymers 303 (2023) 120464

Contents lists available at ScienceDirect

Carbohydrate Polymers

journal homepage: www.elsevier.com/locate/carbpol

Cellulose nanocrystals *vs.* cellulose nanospheres: A comparative study of cytotoxicity and macrophage polarization potential

Dinesh K. Patel [a,1], Keya Ganguly [a,1], Sayan Deb Dutta [a], Tejal V. Patil [b], Ki-Taek Lim [a,b,*]

[a] Department of Biosystems Engineering, Institute of Forest Science, Kangwon National University, Chuncheon 24341, Republic of Korea
[b] Interdisciplinary Program in Smart Agriculture, Kangwon National University, Chuncheon 24341, Republic of Korea

ARTICLE INFO

Keywords:
Shape-regulated nanocellulose
Macrophage polarization
Transcriptome analysis

ABSTRACT

Nanocellulose application has been increasing owing to its appealing physicochemical properties. Monitoring of the crystallinity, surface topography, and reactivity of this high-aspect-ratio nanomaterial is crucial for efficient tissue engineering. Controlling macrophage polarization phenotype remains a challenge in regenerative medicine and tissue engineering. Herein, we monitored the effects of shape-regulated (rod and spherical) nanocellulose on the macrophage modulatory potential of RAW 246.7 cells *in vitro*. Spherical nanocellulose (s-NC) exhibited higher thermal stability and biocompatibility than rod nanocellulose. Macrophage polarization was profoundly affected by nanocellulose topography and incubation period. M2 polarization was observed *in vitro* after 1 day of treatment with s-NC, followed by M1 polarization after treatment for longer periods. Transcriptome analysis similarly revealed that M1 polarization was dominant after 1 day h of incubation with both nanocellulose types. These findings demonstrate that macrophage polarization can be controlled by selecting suitable nanocellulose shape and incubation time for desired applications.

1. Introduction

The success of a given tissue engineering approach is greatly influenced by the host immune system. The host immune response, which is activated within a few hours following the implantation of biomaterials, regulates their fate (Zhao et al., 2022). Therefore, implanted biomaterials with favorable immune responses can facilitate bone regeneration (Batool et al., 2021; Zhu et al., 2021). Macrophages are immune cells that play an important role in inflammation and wound healing (Luu et al., 2015). They are susceptible to changes in the microenvironment surrounding implanted biomaterials and exhibit a wide range of phenotypes (Rostam et al., 2016). M1 (classically activated) and M2 (alternatively activated) are the two widely reported macrophage phenotypes, and their polarization is profoundly influenced by the physicochemical and topographical properties of implanted biomaterials (Rostam et al., 2015). M1 macrophages exhibit pro-inflammatory and anti-tumor effects, whereas M2 macrophages have anti-inflammatory and wound-healing properties. Thus, macrophage polarization and the balance between M1 and M2 are necessary for improved tissue regeneration. Giant body cell formation occurs in response to inappropriate polarization, reducing the effectiveness of implanted biomaterials (Zhang et al., 2020). M1 polarization can be achieved by treating monocyte cells with lipopolysaccharide, whereas M2 polarization can be accomplished by treating monocyte cells with interleukin (IL)-4 or IL-13 (Proost et al., 2014; Verreck et al., 2004). M1 macrophages facilitate the production of various pro-inflammatory cytokines, including IL-6, IL-12, IL-1β, IL-23, and tumor necrosis factor-alpha (TNF-α), and upregulate the expression of chemokine (C—C motif) receptor 2 (CCR2), CCR7, and inducible nitric oxide synthase (iNOS) (Cantero-Navarro et al., 2021; Viola et al., 2019). M2 macrophages trigger the secretion of various anti-inflammatory cytokines, including IL-10 and transforming growth factor (TGF- β) (Miki et al., 2021).

The development of biocompatible biomaterials for regenerative tissues has attracted considerable interest. Various materials, such as chitosan, poly (lactic acid), collagen, alginate, hyaluronic acid, and nanocellulose, have been widely used in tissue engineering applications owing to their attractive physicochemical properties and superior biocompatibility (Filippi et al., 2020; Luo et al., 2019). Nanocellulose has attracted significant interest in tissue engineering because of its favorable physicochemical properties, including large surface area, mechanical strength, low density, and good biocompatibility. It is a nanoform of repeating cellulose units connected by β-1,4-glycosidic

* Corresponding author at: Interdisciplinary Program in Smart Agriculture, Kangwon National University, Chuncheon 24341, Republic of Korea.
E-mail address: ktlim@kangwon.ac.kr (K.-T. Lim).
[1] Equal contributions.

https://doi.org/10.1016/j.carbpol.2022.120464
Received 30 September 2022; Received in revised form 24 November 2022; Accepted 10 December 2022
Available online 14 December 2022

linkages (Chu et al., 2020). Cellulose nanocrystals (CNCs), cellulose nanofibrils (CNFs), and bacterial nanocellulose (BNC) are the three main types of nanocellulose, classified according to their structure and origin. Nanocellulose has distinct physicochemical properties (such as surface area and aspect ratio) and exerts varying effects on immune cells (Ferreira et al., 2020; Luo et al., 2019). Understanding the biomaterial-mediated macrophage polarization process will aid the design and development of materials for tissue engineering. It has been widely established that biomaterial geometrical factors, such as shape, size, and surface chemistry, have significant effects on immune cells (Antmen et al., 2021; Mariani et al., 2019). The effects of CNCs on macrophage polarization have been previously reported, and studies have indicated that CNCs upregulate the expression of inflammatory cytokines, whereas carboxylated CNCs diminish the expression of inflammatory cytokines (Samulin Erdem et al., 2019). However, although nanocellulose shape and size significantly affect macrophage polarization, the effects of shape-regulated nanocellulose on this process have not been reported. Therefore, monitoring the macrophage polarization of shape-regulated nanocellulose would contribute to improved tissue engineering.

Herein, we investigated the effects of shape-regulated nanocellulose (spherical and rod) on the polarization of the murine macrophage cell line RAW 264.7 cells *in vitro*. To the best of our knowledge, this is the first comparative study that analyzed the dependence of macrophage polarization of RAW 264.7 cells on shape-regulated nanocellulose. The obtained nanocellulose was characterized using standard spectroscopic methods. The biocompatibility of shape-regulated nanocellulose was examined with human bone marrow-derived mesenchymal stem cells (hBMSCs) using the WST-8 assay. The mineralization potential of the prepared nanocellulose was also monitored. Transcriptome analysis was conducted to assess the possible macrophage polarization pathways induced by nanocellulose. Based on the obtained results, we hypothesized that nanocellulose geometry, and its properties could be easily determined by selecting suitable chemical reagents for the desired applications.

2. Experimental section

2.1. Materials

All materials were used as obtained without further purifications. Potassium hydroxide (Sigma-Aldrich, St. Louis, MO, USA), sodium hydroxide (Junsei Chemicals, Tokyo, Japan), sodium chlorite, ammonium persulfate (APS) (Daejung Chemicals, Busan, Republic of Korea), acetic acid (99.7 %), sulfuric acid (98.08 %), and hydrochloric acid (35 %) (mass/mass, Wako Chemicals, Osaka, Japan), were used in this experiment. The pine-wood powders (80 mesh, 177 μm) were collected from the local supplier.

2.2. Extraction of spherical nanocellulose and CNCs

Nanocellulose was extracted from pine wood powder through chemical treatment, as described in the Supplementary Information. A process flow diagram for cellulose extraction and purification from pine wood powders is also given in Fig. S1. Spherical nanocellulose (s-NC) was prepared as previously reported, using APS as an oxidizing reagent (Cheng et al., 2014). Briefly, extracted cellulose (5.0 g) was treated with 1 M APS solution at 80 °C for 16 h. After quenching the oxidation using cold water, the mixture was dialyzed using a 12–14 kDa molecular weight cellulose tube against distilled water for 3–4 days. CNCs were extracted using sulfuric acid as the oxidizing reagent.(Sheltami et al., 2012) Cellulose (4.0 g) was then treated with 60 wt% sulfuric acid solution at 45 °C for 50 min with continuous mechanical stirring. Subsequently, the reaction was quenched by adding cold water, followed by dialysis using a 12–14 kDa molecular weight cellulose tube against distilled water for 3–4 days. The samples were then freeze-dried for further analysis. The yields of s-NC and CNCs were 32.2 % and 29.2 %, corresponding to 1.61 and 1.16 g, respectively.

2.3. Spectroscopic characterizations

The morphological characteristics of the extracted nanocellulose were examined by using the field emission transmission electron microscope (FE-TEM) (JEM-2100F, Jeol, Japan) and atomic force microscope (AFM) (Nanoscope 5, Bruker, Germany). The surface charge of the synthesized nanocellulose was measured by using a zeta potential particle size analyzer (Malvern, ZSP, United Kingdom). The Fourier transform infrared (FTIR) spectroscopy (Frontier, Perkin Elmer, UK) was used to assess the presence of the functional groups in s-NC and CNCs in the range of 4000–400 cm^{-1} with a resolution of 4 cm^{-1}. The number of scans was 32 in FTIR measurement. The X-ray diffractometer (X'Pert PRO MPD, Philips, Eindhoven, Netherlands) was explored to evaluate the structural changes in s-NC and CNCs at operating voltage and current of 40 kV and 40 mA, with Cu Kα radiation (λ = 1.5414 A°), respectively. The crystallinity index (CI) of the extracted samples was calculated using the Segal method given in the equation below (Cheng et al., 2014).

$$Crystallinity\ Index\ (CI)\ (\%) = \frac{I_{200} - I_{am}}{I_{200}} \times 100$$

where, I_{200} is peak intensity at (200) diffraction position, and I_{am} is minimum intensity between the (200) and (110) diffraction peaks. All intensity values were taken after subtracting the background signal measured without the samples.

The thermal stability of the prepared nanocellulose was evaluated using a thermal analysis system (TA Instruments, SDT Q600) in the range of 40–600 °C with a heating rate of 10 °C/min in the nitrogen atmosphere. The X-ray photoelectron spectrometer (XPS) (K-Alpha^{+}, Thermo Fischer, USA) was utilized to assess the surface chemistry of the prepared nanocellulose. The XPS spectra were recorded using AlKα source at a constant pass energy of 150 eV. The static sample charging of the recorded spectra was corrected with respect to the C_{1s} peak at 284.8 eV.

Inductively Coupled Plasma Optical Emission Spectroscopy (ICP-OES, Agilent 5900, USA) was used to determine the ion (Ca^{2+} & PO_4^{3-})-binding potential of nanocellulose. For this, $CaCl_2$ (100 mM) and phosphate buffer solutions were prepared using 2 % nitric acid solution. The nanocellulose concentrations were taken at 0.1 wt%. The nanocellulose-treated media were filtered after 24 h, and the concentrations of the remaining ions were measured using ICP-OES.

The surface charge densities (carboxylate and sulfate contents) on the prepared nanocellulose were examined through the electric conductivity titration method as described earlier, with some modifications (Saito & Isogai, 2004). Nanocellulose (0.054 g) was added to distilled water (10 mL) and 0.01 M NaCl (0.90 mL), followed by probe sonication for 10 min. The pH of the suspension was adjusted to 2.5–3.0 with 0.1 M HCl and/or 0.01 M NaOH solution. The conductivity curves were plotted against the consumed NaOH, and the endpoint was taken from the curve. The carboxylate and sulfate contents were determined by using the following equation.

$$Carboxylate \Big/ sulfate\ contents\ \left(\frac{m\ mol}{g}\right) = \frac{\Delta V\ C_{NaOH}}{m}$$

where ΔV is the volume of NaOH at the endpoint, C_{NaOH} is the concentration of used NaOH, and m is the mass of nanocellulose used in the titration.

2.4. Cytotoxicity of nanocellulose

The culture processes for hBMSCs, Raw 264.7, and MG-63 are provided in the Supplementary Information. The cytotoxicity of the

extracted nanocellulose was examined with hBMSCs using WST-8 assay method in 96-well plates after 1, 3, and 5 days of treatment. For this, 1×10^4 cells were placed on the surface of nanocellulose and incubated for the desired periods in a 5 % CO_2 incubator at 37 °C. The groups without nanocellulose treatment were taken as control. The old culture media were changed with fresh culture media after 3 days of treatment. After that, 10 μL of WST-8 dye was added to the cultured media, followed by incubation for 2 h to develop the formazan. The developed formazan was collected in a separate plate, and absorbance was measured with a spectrophotometer at 450 nm (Infinite® M Nano 200 Pro, TECAN, Switzerland). All tests were performed in triplicate ($n = 3$), and data are shown at mean optical density (OD) ± standard deviation (SD). Statistical significance was considered at $^*p < 0.05$. The cytotoxicity of the extracted nanocellulose with RAW 246.7 was also examined in a similar process as described above.

2.5. Cell morphology

The morphological characteristics of hBMSCs with nanocellulose were examined by using an inverted fluorescence microscope (DMi8 Series, Leica Microsystems, Germany) after 3 days of treatment. For this, the cells (2.0×10^4) were placed on the surface of nanocellulose and incubated for the desired periods. The groups without nanocellulose treatment were considered as control. After incubation, the cells were washed with PBS and treated with 4 % paraformaldehyde (PFA) (Sigma-Aldrich, USA) solution, followed by washing with PBS. The cells were then treated with 0.1 % Triton-X 100 for 10 min, and after that, they were incubated with 1 % bovine serum albumin (BSA) (Sigma-Aldrich, USA) for 60 min, followed by staining with 200 μL of Alexa Flor 488-conjugated Phalloidin (F Actin Probe; Invitrogen, Thermo-Fischer Scientific, USA) for 20 min. The nuclei were stained by using 4, 6-diamino-2-phenylindole dihydrochloride (DAPI) (Sigma-Aldrich, USA) for 5 min. These cells were then treated with PBS to remove the excess stains and mounted by adding 1 drop of Prolong® Antifade mounting media (Invitrogen, Thermo-Fischer Scientific, USA). The morphological images were taken with the microscope.

2.6. Mineralization and ALP activity of nanocellulose

The mineralization efficiency of the extracted nanocellulose was examined by the Alizarin red staining (ARS) method after 7 and 14 days of treatment. For this, the cells (4.0×10^4) were placed on the surface of nanocellulose and incubated for the desired periods. The old osteogenic media were replaced with fresh osteogenic media every 3 days. The groups without nanocellulose treatment were taken as control. After incubation, the cells were washed with PBS solution and treated with 4 % PFA solution at room temperature for 15 min to fix the cells, followed by washing with distilled water. Next, the cells were stained with 40 mM ARS (pH 4.2) solution and left for 30 min, and after that, the excess stains were eliminated by washing with distilled water. The photographs of the formed minerals were taken using a light microscope (Zeiss Optical Microscope, USA). A de-staining solution containing 10 % of cetylpyridinium chloride and 10 nM of sodium phosphate (Sigma-Aldrich, USA) was used to quantify the formed minerals. For this, the stained cells were treated with the de-staining solution, and absorbance was recorded at 562 nm by using a spectrophotometer. All the experiments were accomplished in triplicate ($n = 3$), and data are presented as mean OD ± SD. Statistical significance was considered at $^*p < 0.05$.

Alkaline phosphatase (ALP) activity of shape-dependent nanocellulose was monitored with hBMSCs after 7 and 14 days of incubation (Patel, Dutta, Ganguly, Kim, & Lim, 2021). Briefly, 4.0×10^4 cells were incubated with nanocellulose for the desired periods. Next, the cells were incubated with human leukocyte alkaline phosphatase kit (Sigma-Aldrich, USA) as per the manufacturer's protocols. The ALP activity was measured by using *p*-nitrophenyl phosphatase, and absorbance was taken at 405 nm using a spectrophotometer.

2.7. Shape-dependent macrophage polarization potential of nanocellulose

The macrophage polarization effects of the extracted nanocellulose was examined in the presence of RAW 264.7 cells by monitoring morphological changes after 24 h of incubation using a light microscope (Zeiss Optical Microscope, USA). Thus, 2.0×10^4 RAW 264.7 cells were placed on the sample and incubated for the desired period. Groups not subjected to nanocellulose treatment were used as the control. The cells were then washed with phosphate-buffered saline (PBS) and images were captured to visualize the morphological changes in the cultured cells. The morphological changes were also monitored using bright field microscopy. Immunofluorescence (IF) was utilized to examine the morphology of RAW 264.7 cells with prepared nanocellulose after 1, 3, and 5 days of incubation. In brief, 2.0×10^4 cells were incubated with nanocellulose for the desired periods, followed by washing with PBS, and fixing with 3.7 % PFA solution for 15 min. The fixed cells were permeabilized using 0.1 % Triton X-100 for 10 min, followed by washing and blocking with 1 % BSA for 60 min. After that, cells were treated with 200 μL Alexa Fluor-555 (F-actin probe) for 30 min. The nuclei were stained with 20 μL DAPI solution (1 mg/mL) for 2 min under dark conditions. The excess stains were removed by washing with PBS and covered with a mounting media and a glass coverslip. The images were captured using a fluorescence microscope at a magnification of 40 × .

IF was used to assess the macrophage polarization effects of the extracted nanocellulose. The expression of various macrophage phenotype markers (CD68, iNOS, CD86, and CD163) in RAW 264.7 cells was examined after 1, 3, and 5 days of incubation with the nanocellulose samples. To achieve this, RAW 264.7 cells (2.0×10^4) were placed on the surface of the nanocellulose and incubated for the desired period in DMEM media. Groups without nanocellulose treatment were used as the control. After incubation, the cells were washed twice with PBS and fixed by successive treatment with 3.7 % PFA solution for 15 min and absolute methanol for 10 min at room temperature. Next, the cells were blocked by treatment with 1 % bovine serum albumin (BSA) solution containing 5 μL Fc blocker (AAT Bioquest, USA) for 60 min. The cells were then incubated with specific antibodies against CD68, iNOS, CD86, and CD 163 at 4 °C for 12 h at a dilution of 1:500, followed by incubation with secondary antibodies (AF-555 and FITC) for 60 min. Excess antibodies were removed by washing with PBS. The nuclei were stained with DAPI at room temperature for 2 min, followed by washing with PBS. The cells were covered with a mounting medium and a glass coverslip. The morphology of the stained cells was analyzed using an inverted fluorescence microscope at a magnification of 40×. All the antibodies were purchased from Santa Cruz Biotechnology (SCBT) Inc. California, USA.

2.8. Transcriptome analysis

Transcriptome analysis was performed to monitor differentially expressed genes (DEGs) (ebiogen Inc. Seoul, South Korea) arising from treatment with the nanocellulose samples. The groups without nanocellulose incubation were used as controls. Total RNA was extracted after 36 h of treatment with RNAzol reagent (Sigma-Aldrich, USA) and used to prepare the standard RNA library. QuantiSeq 3′ mRNA-Seq was performed using a next-generation RNA sequencer (Nova-Seq 6000, PE100 bp, CA, USA) for reference genome (mm 10, data base: UCHC) in *Mus musculus*. The raw data were analyzed using ExDEGA graphic software (ebiogen, Republic of Korea) and normalized to log2. Up- and down-regulated genes with fold changes of ≥2.0 and p values < 0.05 were included in the statistical analysis.

2.9. Antibody array and bioinformatics study

The human cytokine antibody array (C5) was performed to analyze the expression profiles of Raw 264.7 cell secretome with nanocellulose as per the manufacturer's guidelines. The densitometry data were obtained using ImageJ software (National Institutes of Health, USA

(http://imagej.nih.gov/ij/)) and utilized to compare different samples after background deduction and normalization against the positive control spots. The protein-protein interactions among the identified proteins were analyzed using STRING software (www.string-db.org).

2.10. Statistical analysis

Statistical analyses were performed with one-way ANOVA from OriginPro 9.0 software. The data are presented as mean ± SD. The control group was compared with the treated group, and statistical significance was taken at $^{*}p < 0.05$, $^{**}p < 0.01$, and $^{***}p < 0.001$.

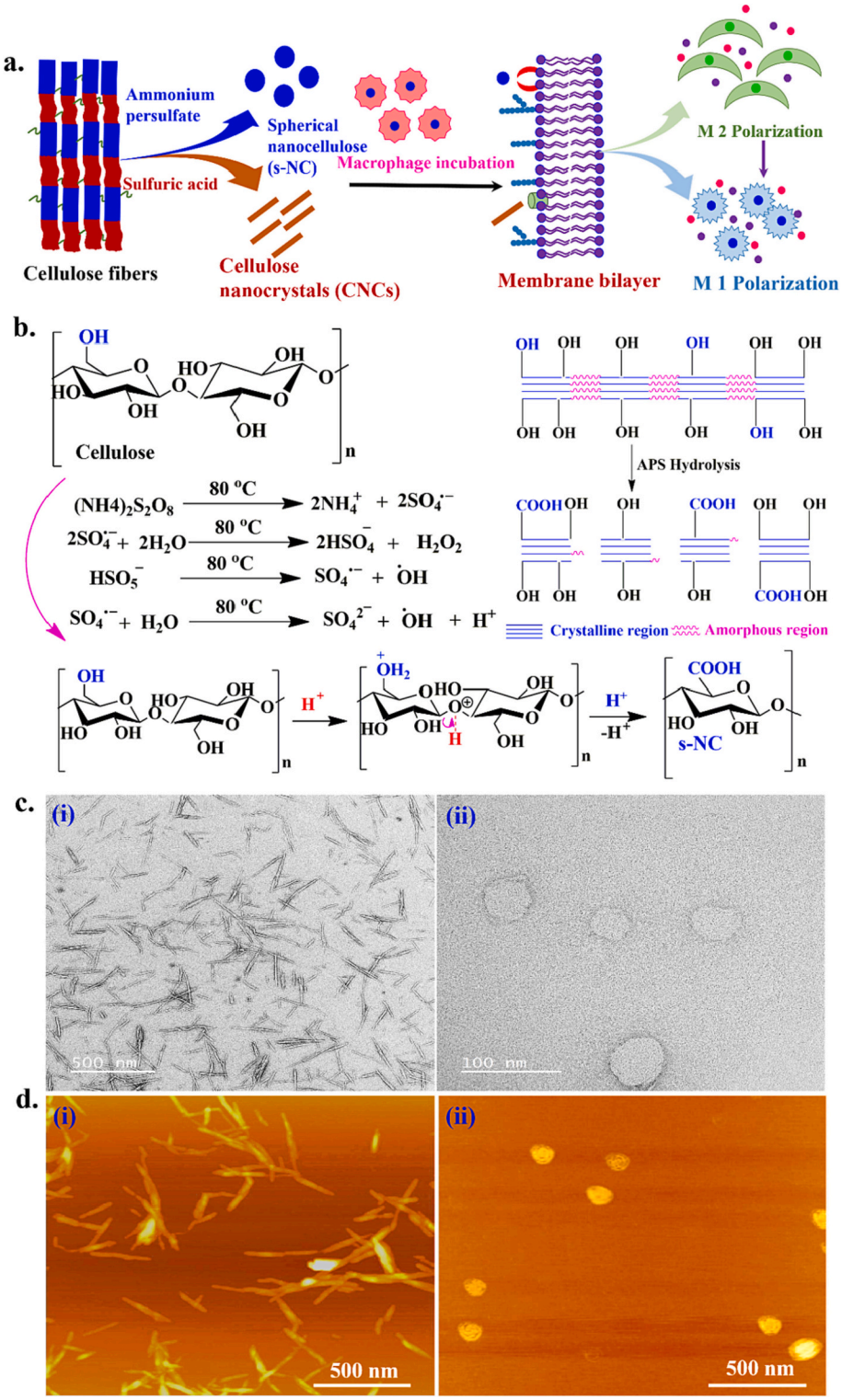

Fig. 1. (a) Schematic representation of the preparation of distinct nanocellulose (NC) samples and their macrophage polarization potential, (b) Proposed pathway for s-NC preparation with APS, (c) TEM images of (i) CNCs, and (ii) s-NC, and (d) AFM images of (i) CNCs, and (ii) s-NC.

3. Results and discussion

3.1. Structural morphologies of extracted nanocellulose

A schematic representation of the extraction of distinct nanocellulose and their ability to induce macrophage polarization is shown in Fig. 1a. APS was used to obtain s-NC from cellulose. It generated nanocellulose from cellulose but also oxidized the C6 hydroxyl groups and converted them into carboxylic groups (Fig. 1b). The principal mechanism of APS method for nanocellulose formation depends on the generation of free radicals ($SO_4^{\bullet-}$), hydrogen peroxide (H_2O_2), and hydrogen sulfate (HSO_4^-) during heating. The generated free radical ions and hydrogen peroxide quickly penetrate the cellulose chains. These chemical moieties accelerate the hydrolysis process and oxidation of C6-hydroxyl groups of cellulose chains. APS also generates H^+ ions during heating, which produces acidic environments in the reaction media. The generated H^+ ions break the glycosylic bonds of cellulose chains, leading to depolymerization similar to acid hydrolysis (Oun & Rhim, 2017; Yang et al., 2020).

The morphologies of extracted CNCs and s-NCs were examined using TEM, and the images are shown in Fig. 1c. The CNCs exhibited a typical needle-like morphological structure with an average length of 140 nm, which was consistent with previously reported values (Jin et al., 2016). The extracted CNCs demonstrated a crystalline morphology, suggesting the effective removal of amorphous regions from their structure during acid hydrolysis. Rounded morphological structures were observed for the APS-hydrolyzed cellulose, verifying the successful generation of s-NC. The diameter of the extracted s-NCs was 43 nm. The changes in the morphology of the extracted nanocellulose under varying oxidizing conditions were also examined using AFM. The AFM images of acid-hydrolyzed and APS-hydrolyzed nanocellulose are shown in Fig. 1d. A typical needle-like morphology with an average length of 150 nm was

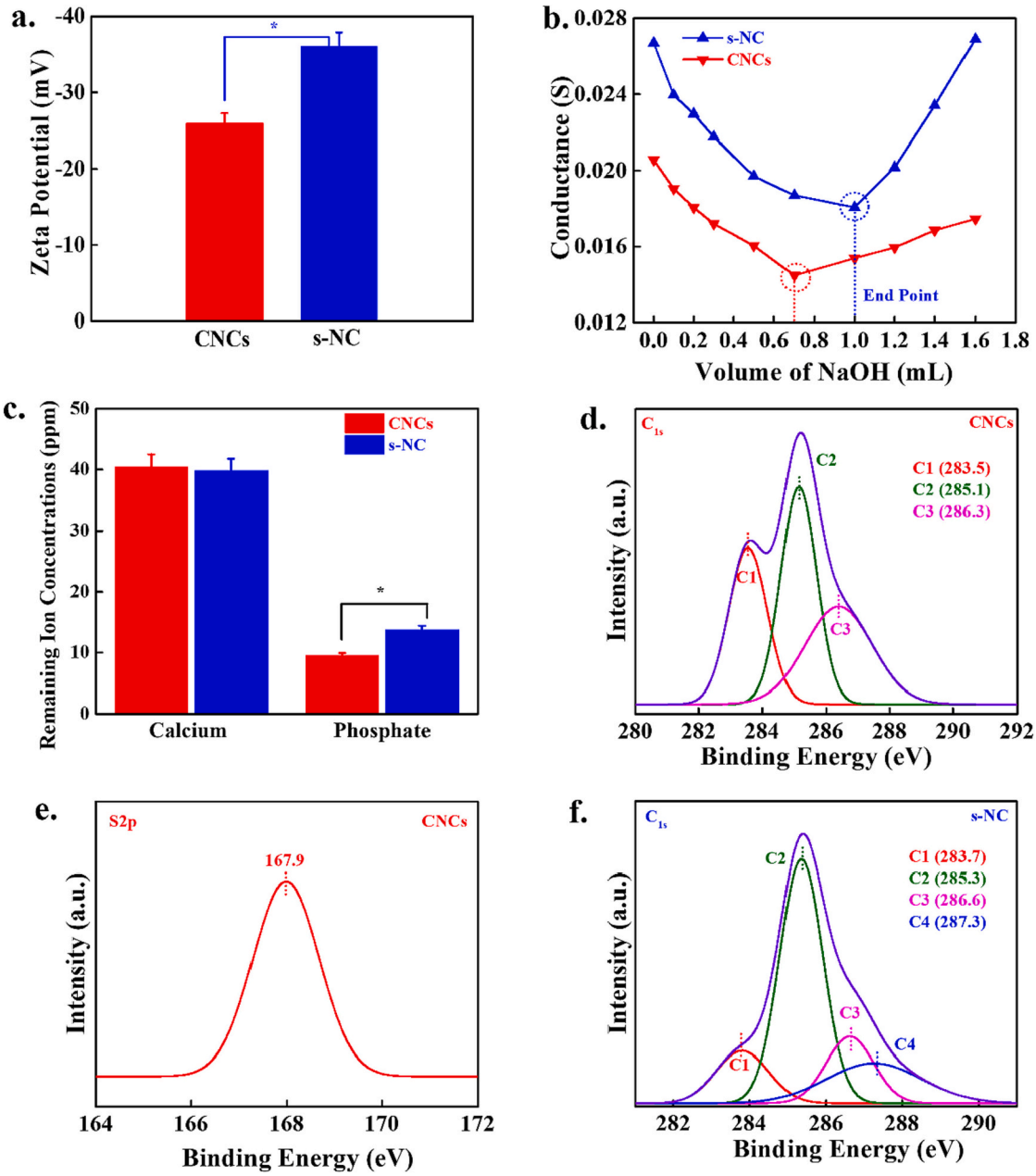

Fig. 2. (a) Zeta potential of the prepared NC, (b) Surface charge on the prepared nanocellulose, (c) Ion adsorption potential of the prepared NC determined using the ICP method, and (d–f) XPS spectra of the indicated nanocellulose in indicated survey regions.

observed in the CNC AFM image, which was consistent with the TEM results. The formation of s-NCs was clearly observed from the AFM image. This phenomenon was attributed to the rapid penetration of the SO_4^- active groups, generated by APS thermal hydrolysis, into the amorphous regions of cellulose resulting in hydrolysis of the 1,4-β glycosidic bonds in the cellulose structures (Lam et al., 2012). Thus, hydrolysis possibly occurred at the surface and inner side of the amorphous zones, leading to the generation of s-NCs.

3.2. Surface potential and functional groups in extracted nanocellulose

The zeta potential (ζ) was measured to examine the surface charge of the extracted nanocellulose generated under varying oxidizing conditions, and the obtained values are presented in Fig. 2a. Surface charge plays a significant role in the stability and re-dispersion of nanomaterials in different solvents. The zeta potentials of CNC and s-NC were −25.9 and −36.0 mV, respectively, suggesting the presence of charged functional groups in their structures. The zeta potential of the CNCs originates from the presence of sulfate ester/sulfonic acid groups resulting from sulfuric acid hydrolysis, and it facilitates the dispersion and stability of CNCs in solvents (Niu et al., 2017). The zeta potential of APS-hydrolyzed s-NC was higher than that of the CNCs, and this may be attributed to the longer duration of oxidation (18 h), which led to the generation of negatively charged functional groups in their structure. Cheng et al. observed a lower zeta potential in nanocellulose from lyocell fibers obtained through APS hydrolysis, compared with that in nanocellulose generated through acid hydrolysis, suggesting that the magnitude of the zeta potential is also affected by the nanocellulose source (Cheng et al., 2014).

We measured the surface charge density of the prepared nanocellulose in terms of sulfate and carboxylate contents by using the electric conductivity titration method, and the results are shown in Fig. 2b. The s-NC showed enhanced conductance potential to CNCs, which could be attributed to the more charged functional groups generated in nanocellulose through APS oxidation and hydrolysis. The surface charges were 0.129, and 0.185 mmol g^{-1} for CNCs and s-NC, respectively. The surface charge, which influences the zeta potential is crucial for nanomaterials stability in suspension and is also a significant factor in the adsorption of nanomaterials on the surface of cells (Rasmussen et al., 2020). It has been observed that carboxylated nanomaterials with a higher surface charge showed greater cellular uptake due to the favorable interactions between carbonyl-rich chains and cell membranes. Hosseinidoust and coworkers assessed the effects of nanocellulose surface charge on the cellular activity of different cells, including HeLa and macrophages, and noted that nanocellulose having surface charge densities above the threshold limits demonstrated cytotoxicity (Hosseinidoust et al., 2015). Therefore, it is believed that nanocellulose generated through APS treatment with a suitable surface charge could significantly accelerate cellular activity, compared with that generated through acid hydrolysis.

Using ICP, we further examined the ion-(Ca^{2+} and PO_4^{3-}) binding potential of the CNCs and s-NC by determining the surface charge on nanocellulose, and the results are shown in Fig. 2c. We examined the concentrations of the ions remaining in the treated media using ICP. A lower concentration of Ca^{2+} ions (39.85 ± 0.14 ppm) was observed for the s-NC-treated groups, compared with that for the CNC (40.0 ± 0.16 ppm) groups in solution, suggesting increased binding of the positively charged Ca^{2+} ions for the former. The lower concentration of Ca^{2+} ions in the s-NC-treated groups could be attributed to the higher zeta potential of s-NC (−36.06 mV), which promoted the adsorption of positively charged ions and decreased their concentration in the media. Furthermore, the phosphate ion concentration was higher in media treated with s-NC (13.71 ± 0.13 ppm) than in the media treated with CNCs (9.45 ± 0.14 ppm). This could be attributed to the high negative zeta potential of s-NC, which made it repel negatively charged phosphate ions.

We also performed the XPS analysis to assess the functional groups in the prepared nanocellulose, and the low-resolution results are given in Fig. S2a–b. The CNCs exhibited survey peaks at 285.3 eV and 533.4 eV, whereas s-NC showed peaks at 285.3 eV and 532.2 eV, which are attributed to the presence of C(1s) and O(1s), respectively. The change in the position of survey peaks of the nanocellulose materials could be attributed to the different electronic environments induced by the functional groups. The high-resolution XPS spectrum of C(1s) of CNCs is shown in Fig. 2d. It can be prominently deconvoluted into three peaks at 283.5, 285.1, and 286.3 eV due to C—C/C—H, C—O, and O—C—O groups, respectively (Abdellah et al., 2018). The high resolution XPS spectrum of S(2p) of CNCs is shown in Fig. 2e. A prominent peak was observed at 167.9 eV, demonstrating the presence of sulfate functional groups through acid hydrolysis in the structure. The high-resolution XPS spectrum of C(1s) of s-NC is given in Fig. 2f. Compared with that of CNCs, the high-resolution XPS spectrum of C(1s) of s-NC was significantly more fitted into four peaks at 283.7, 285.3, 286.6, and 287.3 eV, which could be attributed to the C—C/C—H, C—O, O—C—O, and O—C═O groups, respectively. The additional survey peak at 287.3 eV in s-NC indicated the carboxylate functional groups in the structure. However, no significant peak was observed in the survey regions of 164–175 eV in s-NC, demonstrating the lack of sulfate functional groups in the structure. The high-resolution XPS spectrum of S(2p) of s-NC is shown in Fig. S2c. These results indicate that the nanocellulose functionalities, and consequently their properties, can be tuned by selecting suitable chemical moieties for required applications.

3.3. Chemical structure of extracted nanocellulose

FTIR spectroscopy is a powerful analytical tool used to assess the availability of functional groups in samples. The various functional groups present in the extracted nanocellulose obtained under distinct oxidation conditions were identified using FTIR spectroscopy, and the obtained spectra are shown in Fig. 3a. The characteristic absorption peaks at 3328, 2893, 1633, and 1021 cm^{-1} in the spectra of cellulose, CNCs, and s-NC were attributed to O—H and C—H stretching vibrations, adsorbed water, and C—O functional groups of the polysaccharides, respectively (Aguayo et al., 2018). Furthermore, the extracted cellulose did not give rise to an absorption peak at 1500 cm^{-1}, suggesting the complete removal of non-cellulosic components (lignin) during chemical treatment (Patel, Dutta, Ganguly, & Lim, 2021). The CNCs and s-NC demonstrated absorption peaks similar to those of cellulose, suggesting that no significant structural changes occurred in cellulose under the different oxidizing conditions. The appearance of an additional absorption peak at 1106 cm^{-1} in the spectrum of CNCs was attributed to the presence of sulfate functional groups, originating from acid hydrolysis (Radha et al., 2015). The FTIR spectrum of s-NC exhibited a new absorption peak at 1734 cm^{-1}, indicating the existence of C═O functional groups generated through carboxylation of the cellulose moiety during APS treatment (Cheng et al., 2014). The generation of active carbonyl functional groups by cellulose makes it an attractive nanomaterial for the development of high-performance and flexible composite materials.

Cellulose contains intra- and intermolecular hydrogen linkages, which play a significant role in the assembly of the crystalline structure. The crystalline structures of the extracted cellulose, CNCs, and s-NC, were analyzed using X-ray diffraction analysis, and the obtained patterns are shown in Fig. 3b. Cellulose and s-NC exhibited three diffraction peaks at 11.9°, 20.0°, and 21.5°, suggesting the presence of a cellulose II arrangement in their structure. However, CNCs exhibited diffraction peaks at 14.7°, 16.2°, and 22.5°, indicating the presence of cellulose I in their structure (Kim et al., 2021). It is well known that cellulose presents distinct polymorphic structures, namely cellulose I, II, III, and IV. Of these, cellulose I and II are the most stable and are often used in various applications. Each polymorph has distinct physicochemical properties that depend on the synthesis process (Gong et al., 2017). Thus, acid

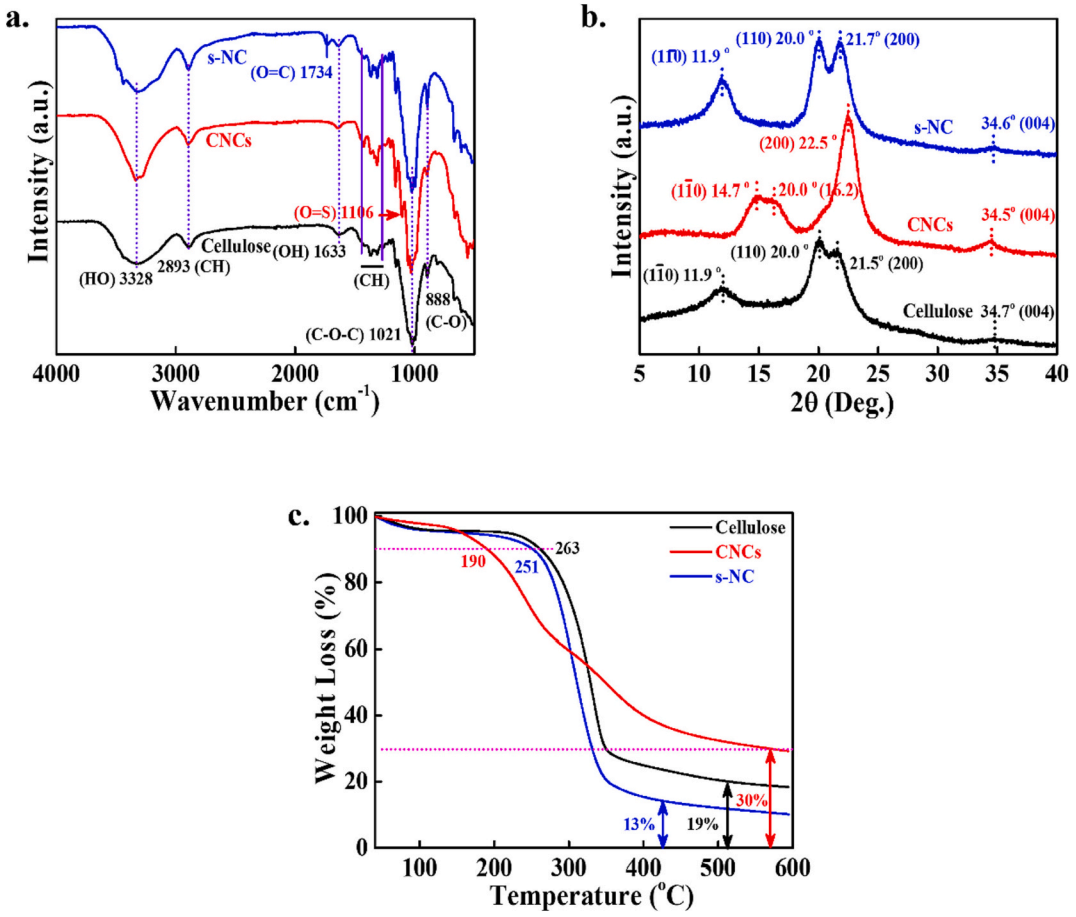

Fig. 3. (a) FTIR spectra, (b) XRD patterns, and (c) TGA curves of the NC samples.

hydrolysis facilitated the formation of cellulose I, whereas APS hydrolysis favored the formation of the cellulose II polymorph structure. The CI values for cellulose, CNCs, and s-NC were 76.19 %, 93.41 %, and 94.01 %, respectively. The CI value of s-NC was slightly higher than that of CNCs, suggesting that greater hydrolysis of the amorphous regions of cellulose occurred through the APS oxidizing reagent than that through sulfuric acid. Therefore, it is possible to obtain nanocellulose with different morphological characteristics and crystallinity by tuning the reaction conditions or reagents used for the synthesis.

The thermal stability of the extracted nanocellulose was analyzed with thermogravimetric analysis (TGA), and the results are shown in Fig. 3c. Cellulose and s-NC exhibited a one-step degradation pattern, whereas CNCs underwent two-step thermal degradation. The degradation temperatures at which 10 % weight loss occurred in cellulose, CNCs, and s-NC were 263, 190, and 251 °C, respectively. The decrease in the thermal stability of CNCs and s-NC, compared with that of cellulose, can be attributed to the presence of heat-sensitive sulfate and carboxylic groups in their backbones, respectively. Heat-sensitive functional groups facilitate the initial degradation process and activation (Nan et al., 2017; Sharma & Varma, 2014). Sulfate groups are more sensitive to heat than carboxylic groups, and hence the sulfate groups have lower thermal stability than the carboxylic groups. The existence of heat-sensitive sulfate and carboxylic functional groups in the CNCs and s-NC was deduced from the FTIR results described above (Fig. 3a). The degradation temperature in the region of 265–410 °C is associated with the cleavage of glycosidic linkages, and is indicative of the degree of polymerization. This process generates carbon dioxide, water vapor, and other chemical moieties. The carbon residues in cellulose, CNCs, and s-NC accounted for 19 %, 30 %, and 13 %, respectively. The higher content of carbon residues in CNCs can be attributed to rapid dehydration resulting from the presence of sulfate groups, and this facilitates increased formation of carbon residues at a higher temperature (Merlini et al., 2020).

3.4. Cytotoxicity of extracted nanocellulose

The cytotoxicity of the extracted nanocellulose was assessed using the WST-8 assay with hBMSCs at various concentrations (20, 40, 60, 80, and 100 μg/100 mL) and specific time intervals, and the results are shown in Fig. 4a and b. The hBMSCs and media not treated with nanocellulose were used as controls. Nanocellulose-treated groups exhibited greater cellular activity than the control after 1 d of treatment. This was further enhanced with incubation time (5 d), indicating favorable conditions for cellular activity (DeLoid et al., 2019). The s-NC-treated groups demonstrated higher cell viability than the CNC-treated groups throughout the incubation period, suggesting their superior biocompatibility. The enhanced cellular activity in the s-NC-treated groups can be attributed to favorable topographical properties of s-NC, compared with those of CNCs, which promoted cellular activity. It is well established that the biological activity of nanomaterials is profoundly affected by their surface chemistry, size, and shape (Bai et al., 2019). Zhang et al. examined the shape-dependent cytotoxicity of poly (lactic-*co*-glycolic acid)/poly (ethylene glycol) (PLGA/PEG) nanoparticles in human cells. They observed that needle-shaped nanoparticles exert significant cytotoxicity toward human cells, compared with their spherical counterparts due to the rupture of the lysosomal membrane (Zhang et al., 2017). Therefore, it is anticipated that s-NC will provide better conditions for cellular activity than its CNCs counterpart. The cell viability was highest at 80 μg/100 mL of s-NC, suggesting that this an optimal concentration for cellular activity. Based on

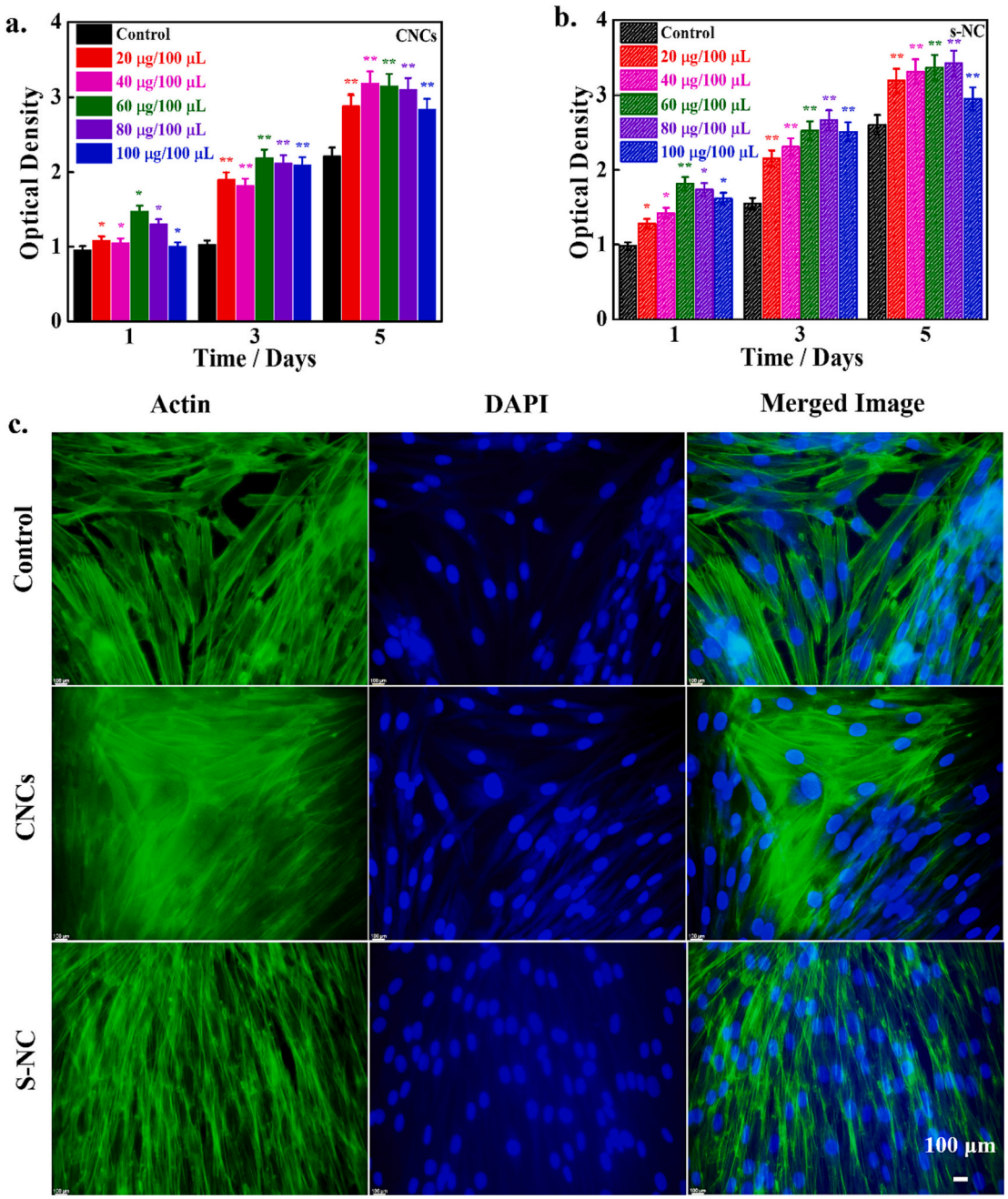

Fig. 4. Cytotoxicity evaluation of the NC samples. Cell viability of hBMSCs treated with (a) CNCs, (b) s-NC at varying concentrations and at indicated periods. (c) Inverted fluorescence microscopy images showing hBMSC morphologies resulting from 3 d of treatment with the indicated NC.

these findings, 80 µg/100 mL of nanocellulose was used for further studies.

The morphological characteristics of the hBMSCs after 3 d of incubation with nanocellulose were examined using a fluorescence microscope, and the obtained images are presented in Fig. 4c. Groups not treated with nanocellulose were used as the control. The cells appeared healthy and elongated in shape and were connected to each other. The cell densities were higher in the nanocellulose-treated groups than in the control group, suggesting that the material has a favorable biocompatibility. Furthermore, cell density was higher in the s-NC-incubated groups than in the CNC-treated groups, indicating the superior cytocompatibility of the former. This finding is consistent with the cell viability results.

3.5. *Mineralization and ALP potentials of nanocellulose*

The mineralization efficiency of the prepared nanocellulose was assessed using the ARS method after 7 and 14 d of incubation with hBMSCs, and the results are shown in Fig. 5a. Groups not treated with nanocellulose were used as the control. We used 80 µg/100 mL of nanocellulose for this study because of the improved cellular activity of hBMSCs at this concentration. A higher degree of mineral nodule formation was observed in the nanocellulose-treated groups than in the control group after 7 d of incubation, demonstrating their superior mineralization potential. Mineralized nodule formation further increased with increasing incubation period (14 d), indicating improved mineralization potential. The improved mineralization in nanocellulose is attributed to the presence of active hydroxyl (–OH) functional groups in its backbone, which facilitates apatite formation through interactions

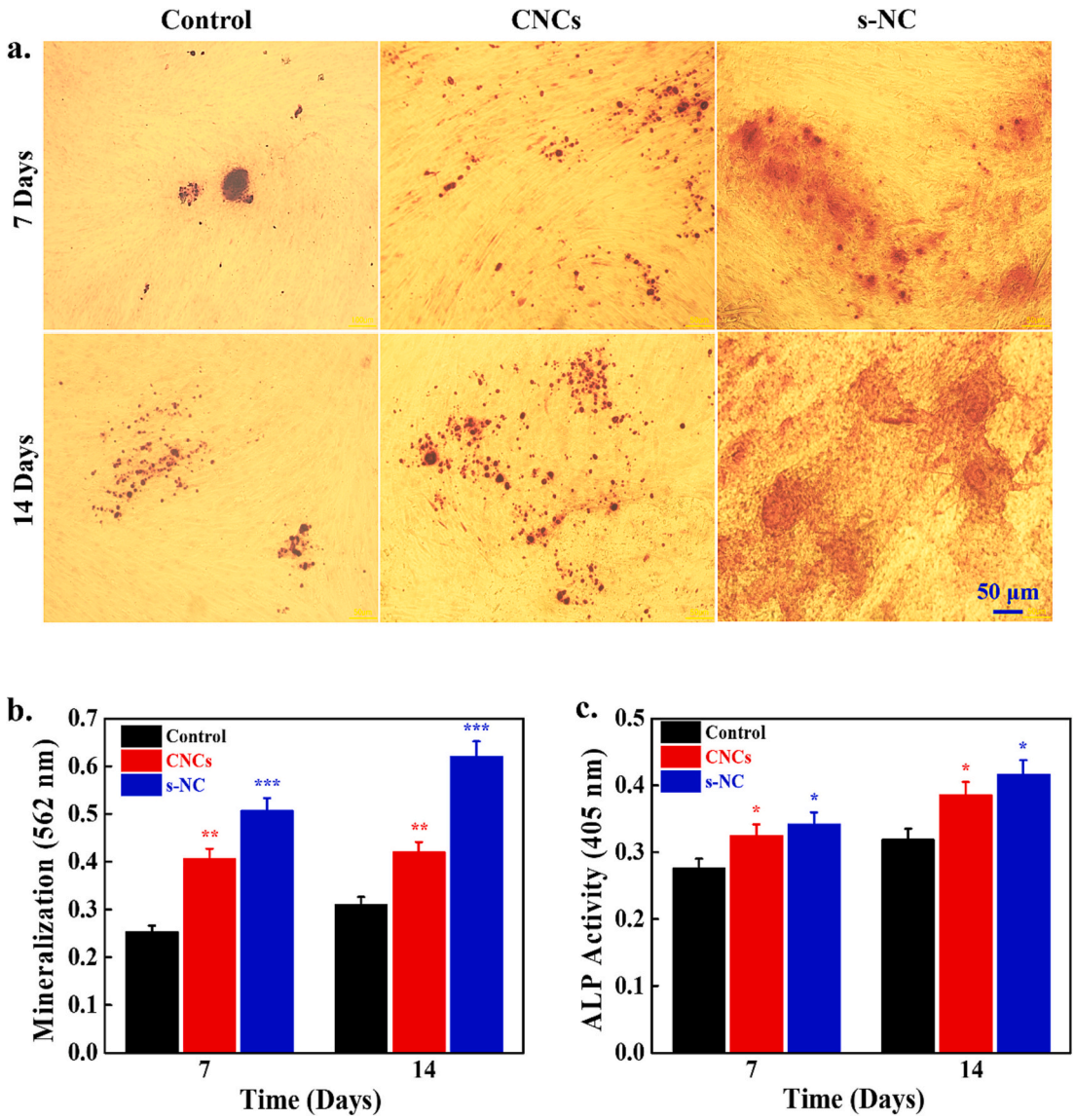

Fig. 5. Mineralization potentials of the developed NCs. (a) Optical images of the minerals formed after 7 and 14 d of incubation with the developed NCs, (b) Quantitative values for the formed minerals, and (c) ALP activity observed after treatment with the developed NCs at indicated periods.

with cations (Chen et al., 2015). A number of factors, such as shape, size, surface topography, and availability of active functional groups in biomaterials, play significant roles in apatite deposition (Patel, Dutta, Shin, Ganguly, & Lim, 2021). The s-NC-treated groups exhibited greater mineral deposition than the CNC-treated groups under all treatment conditions (7 and 14 d), indicating their superior mineralization efficiency. The higher mineralization potential of s-NCs can be attributed to their structural features. A greater concentration of negative charges was present on the surface of NC (ζ, −36.0 mV) than on CNC (−25.9 mV), leading to stronger interactions with cations and increased mineral deposition. Gorgieva et al. reported improved mineral deposition in phosphonated cellulose nanofibers owing to the strong ionic interactions between charged phosphate ions and calcium ions, resulting in enhanced apatite deposition (Gorgieva et al., 2017). The quantitative values of the deposited minerals were also determined, and the results are shown in Fig. 5b. Mineral deposition was higher in the nanocellulose-incubated groups than in the control group after 7 and 14 d of treatment, demonstrating the mineralization enhancing properties of nanocellulose. These results indicated the superior mineralization induction potential of s-NC, suggesting its applicability in bone tissue engineering, as biomaterials used for bone repair and regeneration should facilitate mineralization.

The osteogenic potential of extracted nanocellulose was investigated in terms of ALP activity, to explore its potential use in bone tissue engineering. ALP is considered an important indicator of early-stage osteogenesis (Maturavongsadit et al., 2021). The ALP enzyme activity of hBMSCs after 7 and 14 d of treatment with extracted nanocellulose is shown in Fig. 5c. Groups not treated with nanocellulose treatment were used as the control. We employed 80 µg/100 mL of nanocellulose for this study because of the enhanced cellular activity of hBMSCs at this concentration. Nanocellulose-treated groups showed higher ALP activity than the control after 7 d of incubation, which increased after 14 d of incubation, this demonstrated that nanocellulose has the ability to promote osteogenic differentiation. The higher ALP activity in the presence of nanocellulose can be attributed to the existence of active hydroxyl (—OH) functional groups, which facilitated ALP activity (Guo et al., 2020). Furthermore, the ALP activity was higher in s-NC-treated groups than in those treated with CNCs under all treatment conditions, demonstrating its superior osteogenic differentiation. This distinction can be attributed to the enhanced cellular activity of s-NC-treated hBMSCs. It is well established that ALP activity is profoundly affected by the shape and size of the introduced nanomaterials. Li et al. investigated

the effects of shape- and size-regulated gold nanoparticles (AuNPs) coated with bovine serum albumin on ALP activity. They found that spherical AuNPs promoted ALP activity to a higher extent than the other shapes as a result of improved cellular activity (Li et al., 2016).

3.6. Shape-regulated macrophage polarization of nanocellulose

Evaluating the cytocompatibility of biomaterials is essential for tissue-engineering applications. The cytocompatibility of the extracted nanocellulose was monitored in RAW 264.7 cells after 1 day of treatment, and the results are presented in Fig. 6a. The groups not treated with nanocellulose treatment were used as the control. Herein, we utilized 80 μg/100 mL of nanocellulose to assess their cytocompatibility with RAW 264.7, due to enhanced viability of hBMSCs at this concentration. The nanocellulose-treated groups displayed improved viability than the control, suggesting a positive effect on cell proliferation. The viability of RAW 264.7 cells was higher in s-NC treated groups than in those treated with CNC; hence, s-NC is a superior promoter of cellular activity. The macrophage polarization efficiency of nanocellulose is closely associated with its biocompatibility because macrophages react first upon the incorporation of nanomaterials in cellular environments. The macrophage polarization efficiency of nanocellulose was assessed in RAW 264.7 cells after 1, 3, and 5 days of treatment, and the resulting phase contrast (bright field) morphologies of the cultured RAW 264.7 cells are shown in Fig. 6b. The media devoid of nanocellulose were used as the control. Herein, we used 80 μg/100 mL of nanocellulose to examine macrophage polarization due to enhanced cellular activity at this concentration. A nearly spherical cell morphology, characteristic of monocyte structures, was observed in the control cells. In contrast, the nanocellulose-treated groups contained some elongated cells, suggesting the polarization-inducing capacity of nanocellulose. Furthermore, the densities of the elongated cells were higher in the s-NC-treated groups than in the CNC-treated groups, demonstrating the superior macrophage (M2) polarization potential of s-NC. Various factors, including the physicochemical properties of implanted biomaterials, local microenvironments, and other signal sources, can significantly influence the differentiation of macrophage phenotypes (Gao et al., 2021). Various nanomaterials, such as metal ions (Ag, Au), metal oxides (ZnO, TiO_2), and carbon nanotubes, have demonstrated the ability to induce macrophage polarization, and most nanomaterials favor M1 polarization (Samulin Erdem et al., 2019). Monocyte polarization occurs after biomaterial implantation or microbial infections. Macrophage polarization from classically activated pro-inflammatory M1 to alternatively activated regenerative M2 is favorable for improved tissue regeneration (Nishiguchi & Taguchi, 2020). The CNC-treated groups predominantly exhibited rounded morphologies, indicative of the M1 phenotype. In contrast, stretched and elongated cell morphologies were observed in s-NC-treated groups, suggesting the occurrence of the M2 phenotype (Rostam et al., 2017). Vereyken et al. described a similar relationship between macrophage activation and morphological changes. They found that M1 macrophages presented rounded and flat morphologies, whereas M2 macrophages exhibited stretched and elongated structures

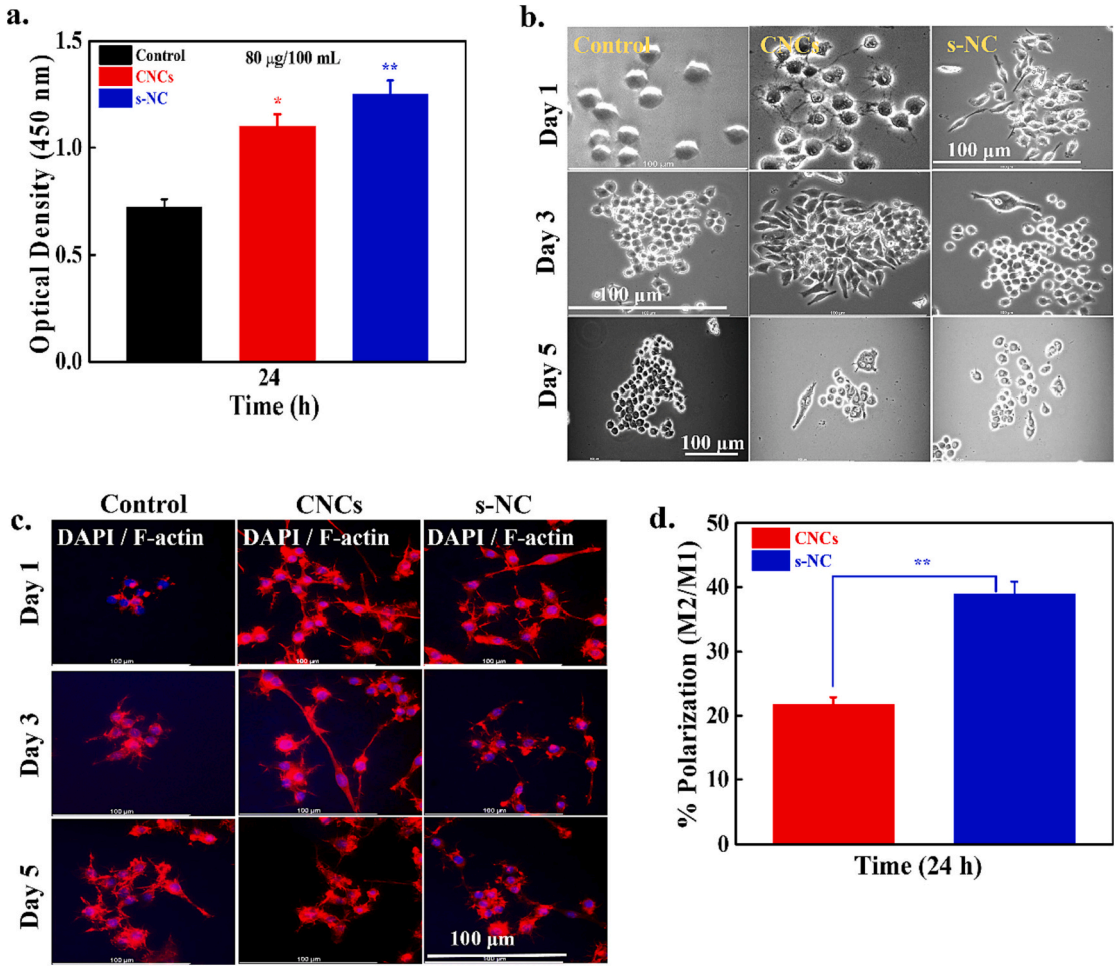

Fig. 6. (a) Cytotoxicity of the developed NCs against RAW 264.7 cells observed after 1 day of incubation, (b) Changes in the morphologies of the cultured RAW 264.7 cells at indicated periods, (c) Actin morphology of the cultured RAW 264.7 cells at indicated periods, and (d) % Polarization of macrophages occurring after 1 day of treatment with both NCs.

(Vereyken et al., 2011). The percentage of M2 macrophage polarization was higher in s-NC-treated groups than in those treated with CNCs after 1 day, indicating the superior macrophage polarization potential of the former.

We determined the aspect ratio (ratio length/width) of the RAW 264.7 cells after 1 day of incubation to examine the morphological changes. The aspect ratio was 1.08, 1.47, and 3.05 for the control, CNCs, and s-NC treated groups, respectively. The higher aspect ratio in s-NC treated groups further suggests elongated morphology of RAW 264.7 cells, which is characteristic morphology for M2 polarization (Mondadori et al., 2023). Therefore, monitoring the changes in cell morphology can help to effectively evaluate the macrophage activation status. We examined the morphological changes after 3 and 5 d of incubation with s-NC and CNC to assess their effects on macrophage polarization. Interestingly, the s-NC-treated groups showed a higher proportion of cells with rounded and flat morphology than those treated with CNCs, and this indicated the superior M1 polarization efficiency of s-NC. M2 polarization potential was only observed with s-NC after 24 h of incubation. The CNC-treated groups contained some flat and elongated cells, indicating M2 polarization ability. These results indicate that macrophage polarization is profoundly affected by the nanomaterial shape and incubation period. To support these findings, we additionally captured the fluorescence images of the RAW 264.7 cells after 1, 3, and 5 days of incubation, and the morphologies are given in Fig. 6c. The groups without nanocellulose treatment were taken as control. The nanocellulose-treated group's exhibit more elongated morphology than the control, showing its polarization ability. The density of elongated cells was high in s-NC treated groups compared to CNCs, indicating its greater M2 polarization potential after 1 day of incubation. Interestingly, the population density of elongated cells was decreased in the s-NC treated group vis-à-vis CNCs groups with increasing incubation periods (3, and 5 days), suggesting its M1 polarization ability. These findings are consistent with the results obtained by the phase contrast images. The change in the morphology of the cultured RAW 264.7 cells was also visualized by optical microscope, and the obtained morphologies are given in Fig. S3. The morphological changes were consistent with the results obtained by the phase contrast images, showing that macrophage polarization was significantly affected by the topography of materials and culture periods. The macrophage polarization ability of nanocellulose was also quantitatively assessed by monitoring the morphological changes (optical images) in the macrophages after 1 day of incubation using ImageJ software. The results are shown in Fig. 6d. The s-NC treated groups show greater M2 polarization tendency than CNCs treated groups after 1 day of incubation.

To further verify the macrophage polarization inducing capacity of the extracted nanocellulose, we examined the expression of different cell markers, including CD63, CD68, iNOS, and CD163 after 1 day treatment using fluorescence microscopy, and the results are shown in Fig. 7a. The groups without nanocellulose incubation were considered as control. CD63, CD68, and iNOS are characteristic cell markers for the M1 phenotype, whereas CD163 is associated with cell markers for M2 phenotype. (Han et al., 2021; Lisi et al., 2017). The expression of CD63, CD68, and iNOS markers was higher in the CNC-treated groups after 1 day of incubation than in the s-NC group, indicating M1 polarization. In contrast, upregulation of the CD163 marker occurred in the presence of s-NC, which is indicative of M2 polarization. Additionally, elongated cell morphologies were also visualized in s-NC treated groups, showing their M2 polarization potential. The staining intensities of CD63, CD68, iNOS, and CD163 markers were measured using ImageJ software, and the corresponding normalized intensities are given in Fig. 7b. The CD63,

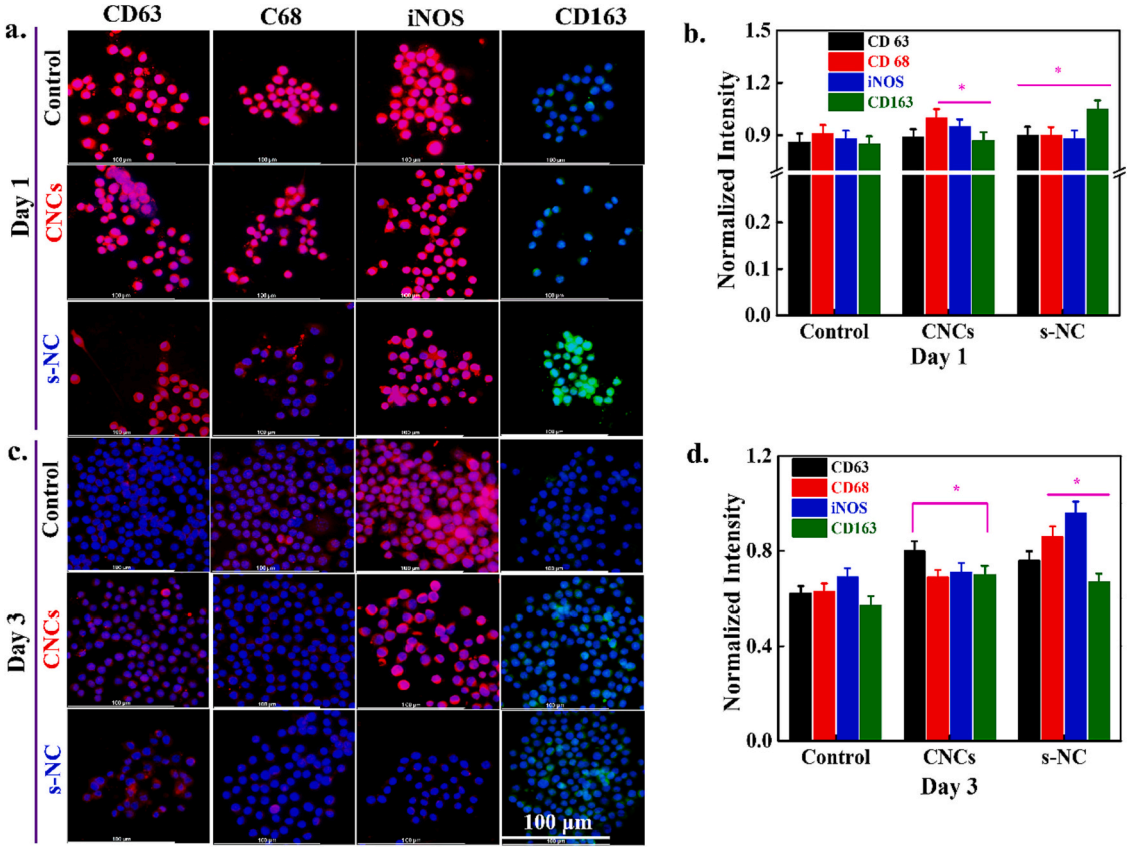

Fig. 7. (a) Immunofluorescence morphologies of RAW 246.7 cells incubated with the indicated NC showing respective surface markers after 1 day of incubation, (b) The quantitative values of the expressed surface marker after 1 day of incubation, (c) Immunofluorescence morphologies of RAW 246.7 cells incubated with the indicated NC showing respective surface markers after 3 days of incubation, and (d) fluorescence intensities of the indicated surface markers observed after 3 days of incubation with the NC samples.

CD68, and iNOS intensities were higher in CNCs treated groups compared to the s-NC treated groups, demonstrating its M1 polarization inducing ability. The CD163 staining intensity was higher in the s-NC-treated groups than in those treated with CNC, indicating its M2 polarization potential. These findings are consistent with the morphological changes observed in macrophages after one day of incubation with the nanocellulose samples, as shown in Fig. 6b. The fluorescence morphologies of the cultured RAW 264.7 cells were also taken after 3 days of incubation and the images are shown in Fig. 7c. The expression of CD63, CD68, and iNOS markers was higher in the s-NC treated groups after 3 days of incubation than CNCs groups, indicating M1 polarization. In contrast, down-regulation of the CD163 marker occurred with s-NC treated groups than CNCs, suggesting the switching of macrophage polarization ability (M2 → M1) of s-NC after 3 days of incubation. The quantitative intensity value of the expressed markers was also determined using ImageJ, and the values are presented in Fig. 7d. A decrease in CD163 intensity was observed in s-NC treated groups than CNCs, demonstrating its switching polarization potential. Purcu and coworkers also observed that the macrophage polarization ability was profoundly affected by the stimulation time (Haziot et al., 2022). We further monitored the effects of macrophage-derived conditioned media (M-CM) on MG-63 cell viability after 1 day of incubation to evaluate the pro-inflammatory behavior, and the results are shown in Fig. S4. Groups not treated with M-CM were used as the control. A decrease in cell viability was observed in the M-CM-treated cells, compared with the control, indicating the inflammatory potential of M-CM. This effect was more pronounced in the case of s-NC M-CM than in CNC M-CM, indicating an enhanced inflammatory response. The decrease in MG-63 cell viability could be attributed to the generation of reactive oxygen species (ROS), which caused cell death. s-NC can possibly induce a higher degree of ROS generation than CNCs due to its greater surface charge. Based on these results, it can be concluded that the nanomaterial shape significantly affects macrophage polarization, and selecting an appropriate shape can contribute to effective tissue engineering.

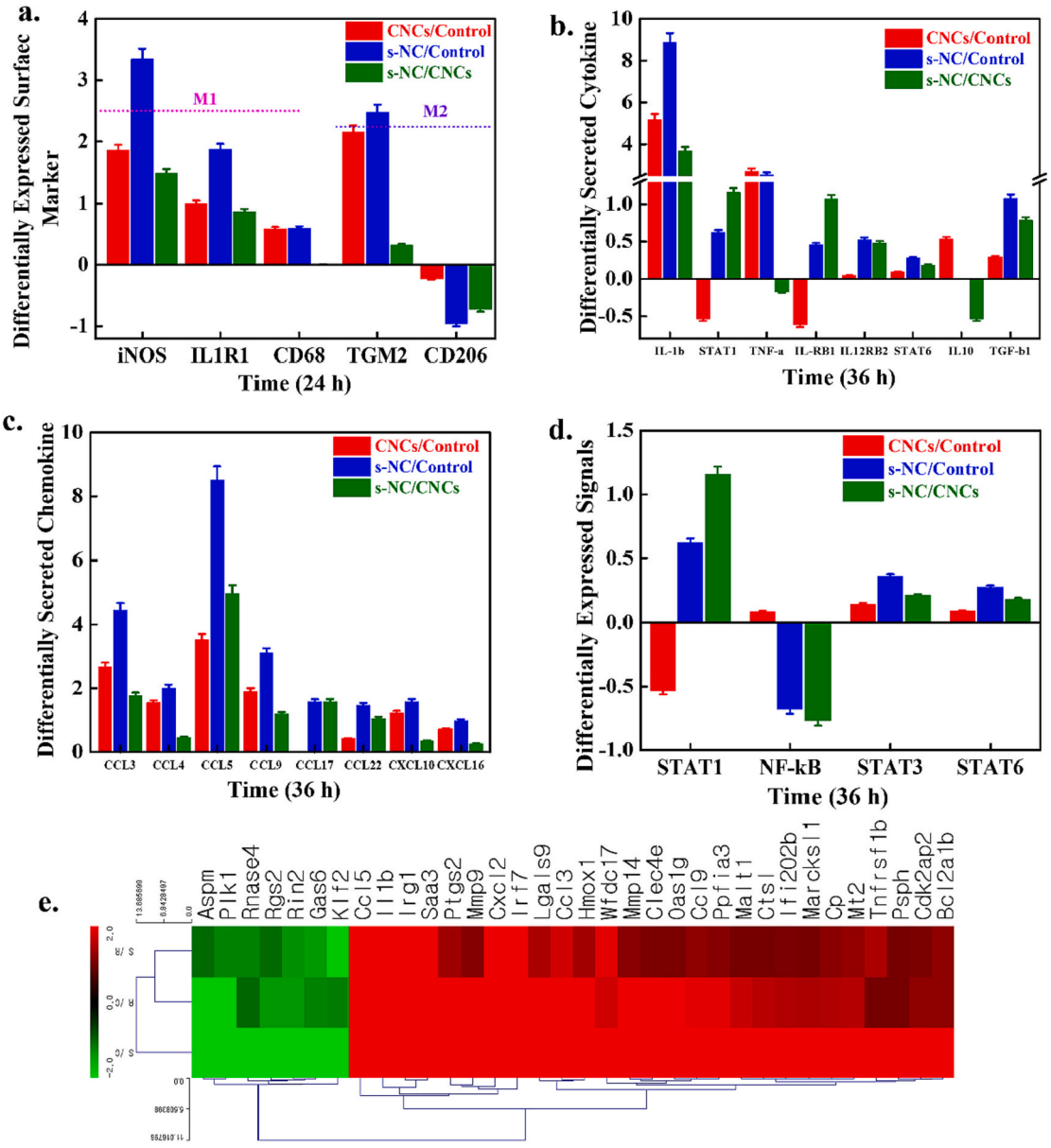

Fig. 8. (a) Transcriptome analysis of differentially expressed macrophage polarized markers, (b) Differentially expressed cytokines, (c) Differentially expressed chemokines, (d) Activation of indicated signaling pathways associated with macrophage polarization, and (e) heat-map profile of the expressed/secreted markers, cytokines or chemokines obtained after 36 h of incubation with both NCs (Statistical analysis were taken $*p < 0.05$).

3.7. Transcriptome analysis

We further performed transcriptome RNA sequencing (RNA-seq) analysis to validate our findings regarding macrophage polarization induced by the distinct nanocelluloses after 36 h of incubation. RNA-seq is a powerful approach for the precise quantification of differentially expressed transcripts, including mRNA, non-coding genes, and proteins (Corchete et al., 2020).

The differentially expressed macrophage-polarization surface markers, including iNOS, IL1R1, CD68, TGM2, and CD206, are shown in Fig. 8a. iNOS and IL1R1 are considered important M1 polarization surface markers and their expression was significantly higher in s-NC-treated groups than in the CNC-treated groups and the control, demonstrating that the spherical topology of nanocellulose favors M1 polarization to a higher degree than its rod counterpart. TGM2, an M2 polarization surface marker, was also upregulated, but its expression level was lower than that of iNOS. CD206, an important M2 marker, was significantly downregulated in the s-NC-treated groups than in the CNC-treated groups, indicating its non-M2 polarization ability. Macrophage polarization is profoundly affected by various factors, such as local microenvironments, nanomaterial stiffness, porosity, and topography (Yunna et al., 2020). The greater M1 polarization capacity of s-NC, compared with that of CNCs, is attributed to its topography and higher negative surface charge. The highly negatively charged s-NC possibly adsorbed the positively charged ions/groups from the DMEM medium, as observed in the ICP-OES results, leading to the creation of a positively charged layer over the s-NC surface. The macrophage surface is negatively charged, attracting positively charged moieties. Therefore, the uptake of s-NC was higher than that of CNCs, which triggered M1 polarization. Initially (within 24 h), M2 polarization occurred with s-NC treatment, and this can be attributed to the reduced uptake of s-NC, which stimulates the macrophages toward M2 polarization (Reichel et al., 2019). Therefore, understanding the mechanisms through which nanomaterials affect the inflammatory response and macrophage polarization will contribute to the development of an effective strategy for improving tissue engineering.

We analyzed the secretion levels of various M1 and M2 cytokines, including IL-1β, STAT 1, TNF-α, IL-RB1, IR12RB2, STAT6, IL10, and TGF-β1, in the presence of the two nanocellulose samples (Fig. 8b). IL-1β and STAT1 are secreted during M1 macrophage polarization, and their secretion levels were significantly higher in the s-NC-treated groups than in the CNC-treated and control groups. The enhanced secretion of these cytokines was attributed to increased M1 macrophage polarization (Fig. 8a). IL10 and TGF-β1 are important cytokines secreted during M2 polarization. These cytokines were also secreted by the nanocellulose-treated groups. However, their secretion levels were significantly lower than those of IL-1β and STAT1 cytokines for both nanocellulose types, suggesting macrophage polarization toward the M1 phenotype. We examined the secreted chemokines (C—C motif) ligand (CCL), including CCL3, CCL4, CCL5, CCL9, CCL17, CCL22, CXCL10, and CXCL16, in the presence of each nanocellulose (Fig. 8c). Chemokines are considered crucial markers for characterizing macrophage polarization. Chemokines CCL3–5 and CCL9 are expressed during M1 macrophage polarization, whereas CCL17, CCL22, CXCL10, and CXCL16 are associated with M2 phenotypes (Miao et al., 2017). The expression levels of CCL3, CCL5, and CCL9 were significantly higher in the s-NC-treated groups than in the CNC-treated and control groups. The higher expression levels of these chemokines in s-NC-incubated media further confirmed its M1-polarization-inducing ability.

We further monitored the activated signaling pathways involved in macrophage polarization in the presence of the distinct nanocellulose. The activation of various signaling pathways, including STAT1, NF-kB, STAT3, and STAT6, is shown in Fig. 8d. STAT1 and NF-kB are associated with the activation of M1 macrophages, whereas STAT3 and STAT6 are associated with the activation of the signaling pathways for M2 polarization. The results indicated that nanocellulose predominantly activated STAT1, indicating the activation of M1 signaling pathways. This effect was more pronounced with s-NC than CNCs, which suggested an enhanced triggering of M1 polarization. Previous studies have demonstrated that cellular uptake widely influences macrophage polarization. Yen et al. reported that the macrophage polarization induced by gold (Au) and silver (Ag) nanoparticles differed owing to dissimilar cellular uptake processes (Yen et al., 2009). The heat map profile data for nanocellulose-activated macrophage polarization are presented in Fig. 8e. The overexpression of M1-associated cytokines and chemokines, such as IL-1β, CCL3, CCL5, and CCL9, occurred in the nanocellulose-treated groups, and they were expressed to a greater extent in s-NC-treated groups, indicating that s-NC showed a greater M1 polarization potential than CNCs. Significant downregulation of various markers, including ASPM, PLK1, RNASE4, RGS2, GAS6, and KLF2, was also observed in the nanocellulose-treated groups, demonstrating their suppressor potential toward the markers. These markers play a crucial role in cancer and neurodegenerative diseases. Therefore, it is possible to control macrophage polarization induced by nanocellulose by selecting the appropriate nanocellulose shape and incubation time for desired applications.

3.8. Antibody array and bioinformatics study

We further performed the cytokine antibody array C5 analysis to assess the macrophage polarization ability shape-regulated nanocellulose with RAW 264.7 cells after 5 days of treatment and the results are shown in Fig. 9a. The groups without nanocellulose treatment were considered as control. It is well-known that different cytokines are secreted by the host immune cells with the response of foreign materials. The nanocellulose-treated array membranes show more intense spots compared to the control, demonstrating its polarization potential. The s-NC-treated group's exhibit more intense spots of TNF-α, IL-1α, IL-1β, IL-12, and IP-10 (CXCL 10) than CNCs treated groups. These cytokines and chemokines are upregulated during M1 polarization. It has been previously reported that the M2 macrophage polarization predominantly occurred by downregulating the signals of different cytokines, such as IL-4, Il-10, IL-13, IL-33, and TGF- β. IL-13 directly induces M2 macrophage polarization (Yao et al., 2019). The s-NC-treated groups also showed these spots on the membrane surface. However, their intensities were lower than M1-associated cytokines. The quantitative values of these secreted cytokines are shown (Fig. 9b). The fold changes in secreted cytokines associated with M1 macrophage polarization were greater in s-NC treated groups, demonstrating a higher M1 polarization potential of the treated nanocellulose. The secretion level of IL-13 cytokine is lower in s-NC, which directly triggers the M2 polarization phage, further suggesting its M2 down-regulation potential. These findings are consistent with the cytokines analyzed by transcriptome RNA sequencing (RNA-seq). Additionally enhanced secretion of neurotrophic factors including, BDNF and NT-3 was also observed in s-NC treated groups, which plays significant roles in neurogenesis, remyelination, and brain repair (Li et al., 2017). However, their fold changes were lower than cytokines associated with M1 macrophage polarization. Based on the secreted cytokines/chemokines, we performed the bio information analysis, and the data are shown in Fig. 9c. The responses were related with inflammation, defense, and immunity, which are characteristics of M1 polarization. These findings indicated that M1 polarization has predominantly occurred after 5 days of incubation with s-NC than CNCs.

Furthermore, we examined the activation of receptors, including interferon-gamma (IFN-γ), nucleotide-binding oligomerization domain 2 (NOD2), interferon-induced protein with tetratricopeptide repeats 1 (IFIT1), and RAC-beta serine/threonine-protein kinase-2 (AKT2), in the presence of the two nanocelluloses, and the results are shown in Fig. 10a. IFN-γ, NOD2, and IFIT1 are associated with the activation of M1 signaling pathways, whereas AKT2 is responsible for M2 activation (Ismail, 2020). The activation of M1-associated receptors, IFN-γ, and in

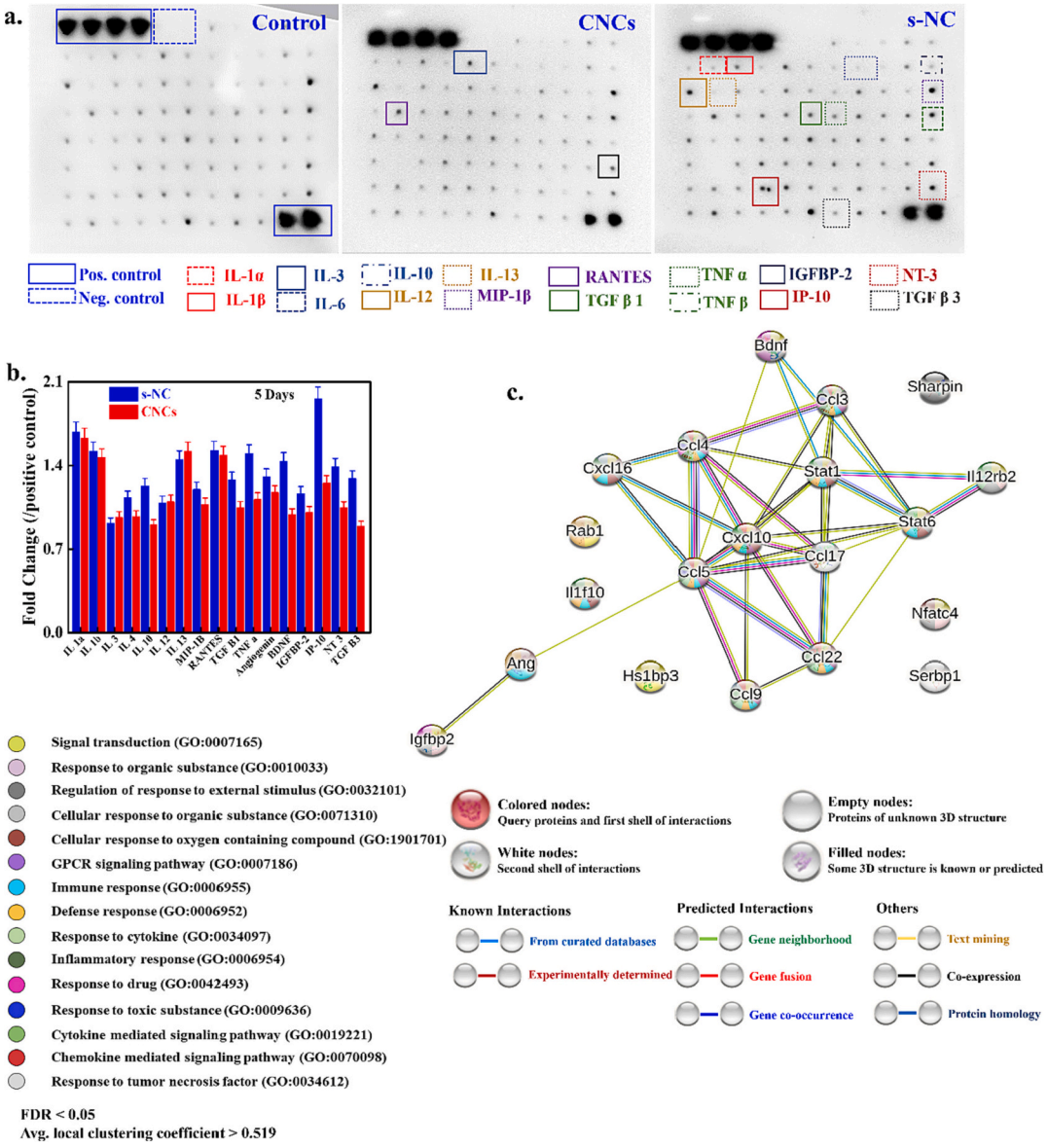

Fig. 9. (a) The proteomic analysis of the secreted cytokines/chemokines with RAW 264.7 cells in the presence of nanocellulose, (b) The quantitative values of the secreted cytokines/chemokines after 5 days of incubation, and (c) The bioinformatics analysis for the secreted cytokines/chemokines after 5 days of treatment.

particular, IFIT1, occurred in the nanocellulose-treated groups and not in the control, indicating the M1-triggering capability of nanocellulose. These receptors were activated to a higher degree in the presence of s-NC than in the presence of CNCs, demonstrating the activation potential of s-NC toward M1 receptors. Based on these findings, a possible mechanism for nanocellulose-induced macrophage polarization is presented in Fig. 10b. The negative zeta potential of s-NC attracts positively charged species, including proteins, resulting in the creation of an electrical double layer, wherein the outer layer is positively charged. The positively charged outer layer interacts with the negatively charged macrophage membrane, leading to the activation of various signaling pathways, such as STAT1 through the IFN-γ receptor and NOD2, which promote M1 macrophage polarization. The highlighted section in Fig. 10c shows a possible M1 polarization pathway. However, further studies are required to validate the postulated mechanism.

4. Conclusion

Nanocellulose is considered a promising nanomaterial for tissue engineering applications owing to its superior physicochemical properties and biocompatibility. Shape-regulated nanocellulose (CNCs and s-NC) was developed from pine wood and characterized using various spectroscopic techniques. Sulfuric acid hydrolysis of pine-wood-derived cellulose facilitated the formation of the cellulose I polymorph, whereas APS hydrolysis favored the formation of cellulose II; the crystallinity indices of the two polymorphs were 93.41 % and 94.01 %, respectively. s-NCs exhibited a higher zeta potential and charge than CNCs. The thermal stability of CNCs was found to be lower than that of s-NC because of the presence of heat-sensitive sulfate functional groups in CNC. The cytocompatibility of extracted CNCs and s-NC was evaluated using hBMSCs, and this was significantly affected by the surface topography and concentration of the nanocellulose materials. Treatment with s-NC resulted in higher cell viability than that with CNC at the same concentration, indicating the superior biocompatibility of s-NC. Enhanced mineralization and ALP activity were observed in the s-NC-treated groups, compared with that in the CNC-treated groups, indicating the osteogenic potential of the former. The macrophage polarization of RAW 264.7 cells was also examined after treatment with the extracted nanocellulose materials, and the results showed that it was profoundly affected by the nanocellulose size. CNCs favored M1

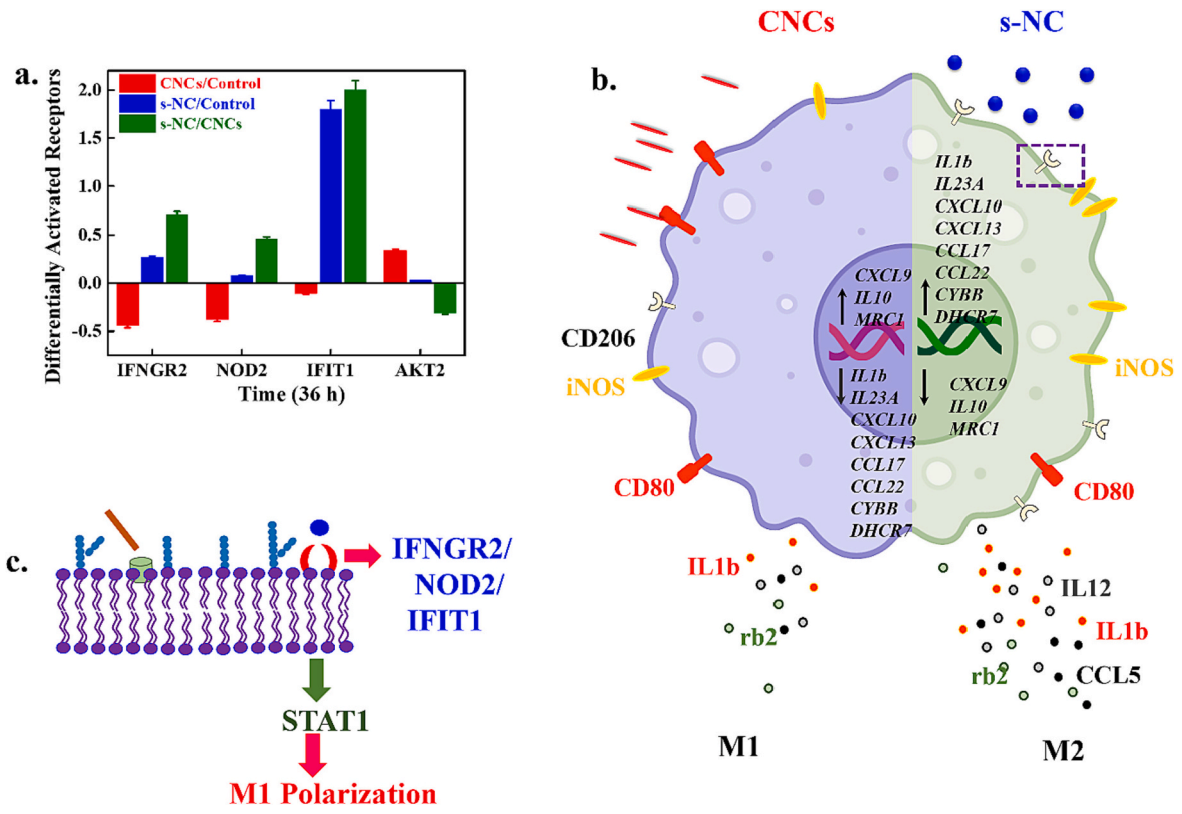

Fig. 10. (a) Transcriptome data for the differential activation of indicated receptors obtained after 36 h of incubation with each NC. (b) A possible NC macrophage polarization mechanism, and (c) magnified view of the indicated area showing possible triggering pathways.

polarization, whereas incubation with s-NC led to M2 polarization after 24 h. However, after prolonged culturing (3 and 5 d) with s-NC, switching of M2 → M1 polarization was observed. M2 polarization is favorable for bone tissue engineering, and hence, selecting nanomaterials with a topography that favors M2 polarization is critical for regenerative tissue applications. Transcriptome analysis data obtained after 36 h of incubation with each of the nanocellulose materials similarly indicated that s-NC is a more effective inducer of M1 polarization than CNCs. Based on these findings, we can conclude that the ability of nanocellulose to induce macrophage polarization is profoundly affected by its physicochemical properties, including shape and surface charge, as well as by the incubation period. A significant decrease in MG-63 cell viability occurred in s-NC-treated M-CM after 1 day of incubation, demonstrating its pro-inflammatory properties, which contributed to cancer cell death. The biological responses were predominantly associated with inflammation, defense, and immunity, which are characteristics of M1 polarization. The study demonstrated that it is possible to control macrophage polarization by applying appropriate nanocellulose shape and size as well as incubation period. Therefore, we hypothesized that nanocellulose geometry and properties can be easily modified with the appropriate chemical moieties for the required applications. However, more detailed studies, including *in vivo* responses, are required to validate our findings.

CRediT authorship contribution statement

Dinesh K. Patel: Conceptualization, fabrication, characterizations, and writing the manuscript. **Keya Ganguly:** Conceptualization, ALP assay, immunocytochemistry experiments, **Sayan Deb Dutta:** Cytotoxicity, **Tejal V. Patil:** Cytotoxicity, and proteomic, and **Ki-Taek Lim:** Supervision, funding acquisition, project administration, and review and editing.

Declaration of competing interest

The authors declare that they have no known competing financial interests or personal relationships that could have appeared to influence the work reported in this paper.

Data availability

Data will be made available on request.

Acknowledgments

The Basic Science Research Program supported this work through the National Research Foundation of Korea (NRF) funded by the Ministry of Education (nos. 2018R1A6A1A03025582, 2019R1D1A3A03103828, & 2022R1I1A3063302), Republic of Korea.

Appendix A. Supplementary data

Supplementary data to this article can be found online at https://doi.org/10.1016/j.carbpol.2022.120464.

References

Abdellah, M. H., Pérez-Manríquez, L., Puspasari, T., Scholes, C. A., Kentish, S. E., & Peinemann, K.-V. (2018). Effective interfacially polymerized polyester solvent resistant nanofiltration membrane from bioderived materials. *Advanced Sustainable Systems, 2*, Article 1800043.

Aguayo, M., Fernández Pérez, A., Reyes, G., Oviedo, C., Gacitúa, W., Gonzalez, R., & Uyarte, O. (2018). Isolation and characterization of cellulose nanocrystals from rejected fibers originated in the Kraft pulping process. *Polymers, 10*, 1145.

Antmen, E., Vrana, N. E., & Hasirci, V. (2021). The role of biomaterials and scaffolds in immune responses in regenerative medicine: Macrophage phenotype modulation by biomaterial properties and scaffold architectures. *Biomaterials Science, 9*, 8090–8110.

Bai, X., Wang, S., Yan, X., Zhou, H., Zhan, J., Liu, S., Sharma, V. K., Jiang, G., Zhu, H., & Yan, B. (2019). Regulation of cell uptake and cytotoxicity by nanoparticle core under the controlled shape, size, and surface chemistries. *ACS Nano, 14*, 289–302.

Batool, F., Özçelik, H., Stutz, C., Gegout, P.-Y., Benkirane-Jessel, N., Petit, C., & Huck, O. (2021). Modulation of immune-inflammatory responses through surface modifications of biomaterials to promote bone healing and regeneration. *Journal of Tissue Engineering, 12*, Article 204173142110414.

Cantero-Navarro, E., Rayego-Mateos, S., Orejudo, M., Tejedor-Santamaria, L., Tejera-Muñoz, A., Sanz, A. B., Marquez-Exposito, L., Marchant, V., Santos-Sanchez, L., Egido, J., Ortiz, A., Bellon, T., Rodrigues-Diez, R., & Ruiz-Ortega, M. (2021). Role of macrophages and related cytokines in kidney disease. *Frontiers in Medicine, 8*, 3389.

Chen, Q., Garcia, R. P., Munoz, J., Pérez de Larraya, U., Garmendia, N., Yao, Q., & Boccaccini, A. R. (2015). Cellulose nanocrystals-bioactive glass hybrid coating as bone substitutes by electrophoretic co-deposition: In situ control of mineralization of bioactive glass and enhancement of osteoblastic performance. *ACS Applied Materials & Interfaces, 7*, 24715–24725.

Cheng, M., Qin, Z., Liu, Y., Qin, Y., Li, T., Chen, L., & Zhu, M. (2014). Efficient extraction of carboxylated spherical cellulose nanocrystals with narrow distribution through hydrolysis of lyocell fibers by using ammonium persulfate as an oxidant. *Journal of Materials Chemistry A, 2*, 251–258.

Chu, Y., Sun, Y., Wu, W., & Xiao, H. (2020). Dispersion properties of nanocellulose: A review. *Carbohydrate Polymers, 250*, Article 116892.

Corchete, L. A., Rojas, E. A., Alonso-López, D., De Las Rivas, J., Gutiérrez, N. C., & Burguillo, F. J. (2020). Systematic comparison and assessment of RNA-seq procedures for gene expression quantitative analysis. *Scientific Reports, 10*, 19737.

DeLoid, G. M., Cao, X., Molina, R. M., Silva, D. I., Bhattacharya, K., Ng, K. W., Loo, S. C. J., Brain, J. D., & Demokritou, P. (2019). Toxicological effects of ingested nanocellulose in in vitro intestinal epithelium and in vivo rat models. *Environmental Science: Nano, 6*, 2105–2115.

Ferreira, F. V., Otoni, C. G., De France, K. J., Barud, H. S., Lona, L. M. F., Cranston, E. D., & Rojas, O. J. (2020). Porous nanocellulose gels and foams: Breakthrough status in the development of scaffolds for tissue engineering. *Materials Today, 37*, 126–141.

Filippi, M., Born, G., Chaaban, M., & Scherberich, A. (2020). Natural polymeric scaffolds in bone regeneration. *Frontiers in Bioengineering and Biotechnology, 8*, 3389.

Gao, Q., Rhee, C., Maruyama, M., Li, Z., Shen, H., Zhang, N., Utsunomiya, T., Huang, E. E., Yao, Z., Bunnell, B. A., Lin, H., Tuan, R. S., & Goodman, S. B. (2021). The effects of macrophage phenotype on osteogenic differentiation of MSCs in the presence of polyethylene particles. *Biomedicines, 9*, 499.

Gong, J., Li, J., Xu, J., Xiang, Z., & Mo, L. (2017). Research on cellulose nanocrystals produced from cellulose sources with various polymorphs. *RSC Advances, 7*, 33486–33493.

Gorgieva, S., Girandon, L., & Kokol, V. (2017). Mineralization potential of cellulose-nanofibrils reinforced gelatine scaffolds for promoted calcium deposition by mesenchymal stem cells. *Materials Science and Engineering: C, 73*, 478–489.

Guo, J., Yu, H., & Cui, T. (2020). Applications of fluorescent materials in the detection of alkaline phosphatase activity. *Journal of Biomedical Materials Research Part B: Applied Biomaterials, 109*, 214–226.

Han, X., Li, W., Li, P., Zheng, Z., Lin, B., Zhou, B., Guo, K., He, P., & Yang, J. (2021). Stimulation of α7 nicotinic acetylcholine receptor by nicotine suppresses decidual M1 macrophage polarization against inflammation in lipopolysaccharide-induced preeclampsia-like mouse model. *Frontiers in Immunology, 12*, 3389.

Haziot, A., Unuvar Purcu, D., Korkmaz, A., Gunalp, S., Helvaci, D. G., Erdal, Y., Dogan, Y., Suner, A., Wingender, G., & Sag, D. (2022). Effect of stimulation time on the expression of human macrophage polarization markers. *Plos One, 17*, Article 0265196.

Hosseinidoust, Z., Alam, M. N., Sim, G., Tufenkji, N., & van de Ven, T. G. M. (2015). Cellulose nanocrystals with tunable surface charge for nanomedicine. *Nanoscale, 7*, 16647–16657.

Ismail, I. A.a. N. (2020). M1 and M2 macrophages polarization via mTORC1 influences innate immunity and outcome of ehrlichia infection. *Journal of Cellular Immunology, 2*, 108–115.

Jin, E., Guo, J., Yang, F., Zhu, Y., Song, J., Jin, Y., & Rojas, O. J. (2016). On the polymorphic and morphological changes of cellulose nanocrystals (CNC-I) upon mercerization and conversion to CNC-II. *Carbohydrate Polymers, 143*, 327–335.

Kim, M., Pierce, K., Krecker, M., Bukharina, D., Adstedt, K., Nepal, D., Bunning, T., & Tsukruk, V. V. (2021). Monolithic chiral nematic organization of cellulose nanocrystals under capillary confinement. *ACS Nano, 15*, 19418–19429.

Lam, E., Leung, A. C. W., Liu, Y., Majid, E., Hrapovic, S., Male, K. B., & Luong, J. H. T. (2012). Green strategy guided by Raman spectroscopy for the synthesis of ammonium carboxylated nanocrystalline cellulose and the recovery of byproducts. *ACS Sustainable Chemistry & Engineering, 1*, 278–283.

Li, J., Li, J. E. J., Zhang, J., Wang, X., Kawazoe, N., & Chen, G. (2016). Gold nanoparticle size and shape influence on osteogenesis of mesenchymal stem cells. *Nanoscale, 8*, 7992–8007.

Li, Y.-H., Xie, C., Zhang, Y., Li, X., Zhang, H.-F., Wang, Q., Chai, Z., Xiao, B.-G., Thome, R., Zhang, G.-X., & Ma, C.-G. (2017). FSD-C10, a fasudil derivative, promotes neuroregeneration through indirect and direct mechanisms. *Scientific Reports, 7*, 41227.

Lisi, L., Ciotti, G. M. P., Braun, D., Kalinin, S., Currò, D., Dello Russo, C., Coli, A., Mangiola, A., Anile, C., Feinstein, D. L., & Navarra, P. (2017). Expression of iNOS, CD163 and ARG-1 taken as M1 and M2 markers of microglial polarization in human glioblastoma and the surrounding normal parenchyma. *Neuroscience Letters, 645*, 106–112.

Luo, H., Cha, R., Li, J., Hao, W., Zhang, Y., & Zhou, F. (2019). Advances in tissue engineering of nanocellulose-based scaffolds: A review. *Carbohydrate Polymers, 224*, Article 115144.

Luu, T. U., Gott, S. C., Woo, B. W. K., Rao, M. P., & Liu, W. F. (2015). Micro- and nanopatterned topographical cues for regulating macrophage cell shape and phenotype. *ACS Applied Materials & Interfaces, 7*, 28665–28672.

Mariani, E., Lisignoli, G., Borzì, R. M., & Pulsatelli, L. (2019). Biomaterials: Foreign bodies or tuners for the immune response? *International Journal of Molecular Sciences, 20*, 636.

Maturavongsadit, P., Narayanan, L. K., Chansoria, P., Shirwaiker, R., & Benhabbour, S. R. (2021). Cell-laden nanocellulose/chitosan-based bioinks for 3D bioprinting and enhanced osteogenic cell differentiation. *ACS Applied Bio Materials, 4*, 2342–2353.

Merlini, A., Claumann, C., Zibetti, A. W., Coirolo, A., Rieg, T., & Machado, R. A. F. (2020). Kinetic study of the thermal decomposition of cellulose nanocrystals with different crystal structures and morphologies. *Industrial & Engineering Chemistry Research, 59*, 13428–13439.

Miao, X., Leng, X., & Zhang, Q. (2017). The current state of nanoparticle-induced macrophage polarization and reprogramming research. *International Journal of Molecular Sciences, 18*, 336.

Miki, S., Suzuki, J.-I., Takashima, M., Ishida, M., Kokubo, H., & Yoshizumi, M. (2021). S-1-propenylcysteine promotes IL-10-induced M2c macrophage polarization through prolonged activation of IL-10R/STAT3 signaling. *Scientific Reports, 11*, 22469.

Mondadori, C., Chandrakar, A., Lopa, S., Wieringa, P., Talò, G., Perego, S., Lombardi, G., Colombini, A., Moretti, M., & Moroni, L. (2023). Assessing the response of human primary macrophages to defined fibrous architectures fabricated by melt electrowriting. *Bioactive Materials, 21*, 209–222.

Nan, F., Nagarajan, S., Chen, Y., Liu, P., Duan, Y., Men, Y., & Zhang, J. (2017). Enhanced toughness and thermal stability of cellulose nanocrystal iridescent films by alkali treatment. *ACS Sustainable Chemistry & Engineering, 5*, 8951–8958.

Nishiguchi, A., & Taguchi, T. (2020). A thixotropic, cell-infiltrative nanocellulose hydrogel that promotes in vivo tissue remodeling. *ACS Biomaterials Science & Engineering, 6*, 946–958.

Niu, F., Li, M., Huang, Q., Zhang, X., Pan, W., Yang, J., & Li, J. (2017). The characteristic and dispersion stability of nanocellulose produced by mixed acid hydrolysis and ultrasonic assistance. *Carbohydrate Polymers, 165*, 197–204.

Oun, A. A., & Rhim, J.-W. (2017). Characterization of carboxymethyl cellulose-based nanocomposite films reinforced with oxidized nanocellulose isolated using ammonium persulfate method. *Carbohydrate Polymers, 174*, 484–492.

Patel, D. K., Dutta, S. D., Ganguly, K., Kim, J. W., & Lim, K. T. (2021a). Enhanced osteogenic potential of unzipped carbon nanotubes for tissue engineering. *Journal of Biomedical Materials Research Part A, 109*, 1869–1880.

Patel, D. K., Dutta, S. D., Ganguly, K., & Lim, K.-T. (2021b). Multifunctional bioactive chitosan/cellulose nanocrystal scaffolds eradicate bacterial growth and sustain drug delivery. *International Journal of Biological Macromolecules, 170*, 178–188.

Patel, D. K., Dutta, S. D., Shin, W.-C., Ganguly, K., & Lim, K.-T. (2021c). Fabrication and characterization of 3D printable nanocellulose-based hydrogels for tissue engineering. *RSC Advances, 11*, 7466–7478.

Proost, P., García, S., Krausz, S., Ambarus, C. A., Fernández, B. M., Hartkamp, L. M., van Es, I. E., Hamann, J., Baeten, D. L., Tak, P. P., & Reedquist, K. A. (2014). Tie2 signaling cooperates with TNF to promote the pro-inflammatory activation of human macrophages independently of macrophage functional phenotype. *PLoS One, 9*, 82088.

Radha, A. V., Lander, L., Rousse, G., Tarascon, J. M., & Navrotsky, A. (2015). Thermodynamic stability and correlation with synthesis conditions, structure and phase transformations in orthorhombic and monoclinic Li2M(SO4)2 (M = Mn, Fe, Co, Ni) polymorphs. *Journal of Materials Chemistry A, 3*, 2601–2608.

Rasmussen, M. K., Pedersen, J. N., & Marie, R. (2020). Size and surface charge characterization of nanoparticles with a salt gradient. *Nature Communications, 11*, 2337.

Reichel, D., Tripathi, M., & Perez, J. M. (2019). Biological effects of nanoparticles on macrophage polarization in the tumor microenvironment. *Nanotheranostics, 3*, 66–88.

Rostam, H. M., Reynolds, P. M., Alexander, M. R., Gadegaard, N., & Ghaemmaghami, A. M. (2017). Image based machine learning for identification of macrophage subsets. *Scientific Reports, 7*, 3521.

Rostam, H. M., Singh, S., Salazar, F., Magennis, P., Hook, A., Singh, T., Vrana, N. E., Alexander, M. R., & Ghaemmaghami, A. M. (2016). The impact of surface chemistry modification on macrophage polarisation. *Immunobiology, 221*, 1237–1246.

Rostam, H. M., Singh, S., Vrana, N. E., Alexander, M. R., & Ghaemmaghami, A. M. (2015). Impact of surface chemistry and topography on the function of antigen presenting cells. *Biomaterials Science, 3*, 424–441.

Saito, T., & Isogai, A. (2004). TEMPO-mediated oxidation of native cellulose. The effect of oxidation conditions on chemical and crystal structures of the water-insoluble fractions. *Biomacromolecules, 5*, 1983–1989.

Samulin Erdem, J., Alswady-Hoff, M., Ervik, T. K., Skare, Ø., Ellingsen, D. G., & Zienolddiny, S. (2019). Cellulose nanocrystals modulate alveolar macrophage phenotype and phagocytic function. *Biomaterials, 203*, 31–42.

Sharma, P. R., & Varma, A. J. (2014). Thermal stability of cellulose and their nanoparticles: Effect of incremental increases in carboxyl and aldehyde groups. *Carbohydrate Polymers, 114*, 339–343.

Sheltami, R. M., Abdullah, I., Ahmad, I., Dufresne, A., & Kargarzadeh, H. (2012). Extraction of cellulose nanocrystals from mengkuang leaves (Pandanus tectorius). *Carbohydrate Polymers, 88*, 772–779.

Vereyken, E. J. F., Heijnen, P. D. A. M., Baron, W., de Vries, E. H. E., Dijkstra, C. D., & Teunissen, C. E. (2011). Classically and alternatively activated bone marrow derived macrophages differ in cytoskeletal functions and migration towards specific CNS cell types. *Journal of Neuroinflammation, 8*, 58.

Verreck, F. A. W., de Boer, T., Langenberg, D. M. L., Hoeve, M. A., Kramer, M., Vaisberg, E., Kastelein, R., Kolk, A., de Waal-Malefyt, R., & Ottenhoff, T. H. M.

(2004). Human IL-23-producing type 1 macrophages promote but IL-10-producing type 2 macrophages subvert immunity to (myco)bacteria. *Proceedings of the National Academy of Sciences, 101*, 4560–4565.
Viola, A., Munari, F., Sánchez-Rodríguez, R., Scolaro, T., & Castegna, A. (2019). The metabolic signature of macrophage responses. *Frontiers in Immunology, 10*, Article 01462.
Yang, T., Qi, H., Liu, P., & Zhang, K. (2020). Selective isolation methods for cellulose and chitin nanocrystals. *ChemPlusChem, 85*, 1081–1088.
Yao, Y., Xu, X.-H., & Jin, L. (2019). Macrophage polarization in physiological and pathological pregnancy. *Frontiers in Immunology, 10*, Article 00792.
Yen, H. J., Hsu, S.h., & Tsai, C. L. (2009). Cytotoxicity and immunological response of gold and silver nanoparticles of different sizes. *Small, 5*, 1553–1561.
Yunna, C., Mengru, H., Lei, W., & Weidong, C. (2020). Macrophage M1/M2 polarization. *European Journal of Pharmacology, 877*, Article 173090.
Zhang, B., Liu, F.-Z., Li, K.-Y., Zou, B., Meng, C.-X., Liu, K., Lv, Z.-Y., Zhang, Y.-J., & Li, J. (2020). The observed difference of macrophage phenotype on different surface roughness of mineralized collagen. *Regenerative Biomaterials, 7*, 203–211.
Zhang, B., Sai Lung, P., Zhao, S., Chu, Z., Chrzanowski, W., & Li, Q. (2017). Shape dependent cytotoxicity of PLGA-PEG nanoparticles on human cells. *Scientific Reports, 7*, 7315.
Zhao, T., Chu, Z., Ma, J., & Ouyang, L. (2022). Immunomodulation effect of biomaterials on bone formation. *Journal of Functional Biomaterials, 13*, 103.
Zhu, Y., Liang, H., Liu, X., Wu, J., Yang, C., Wong, T. M., Kwan, K. Y. H., Cheung, K. M. C., Wu, S., & Yeung, K. W. K. (2021). Regulation of macrophage polarization through surface topography design to facilitate implant-to-bone osteointegration. *Science Advances, 7*, 6654.